

Stony Brook University



OFFICIAL COPY

The official electronic file of this thesis or dissertation is maintained by the University Libraries on behalf of The Graduate School at Stony Brook University.

© All Rights Reserved by Author.

Holographic Pomeron

A Dissertation Presented

by

Alexander Stoffers

to

The Graduate School

in Partial Fulfillment of the Requirements

for the Degree of

Doctor of Philosophy

in

Physics

Stony Brook University

August 2013

Stony Brook University

The Graduate School

Alexander Stoffers

We, the dissertation committee for the above candidate for the Doctor of Philosophy degree, hereby recommend acceptance of this dissertation.

Ismail Zahed – Dissertation Advisor
Professor, Department of Physics and Astronomy

Matthew Dawber – Chairperson of Defense
Assistant Professor, Department of Physics and Astronomy

Derek Teaney
Assistant Professor, Department of Physics and Astronomy

Robert Pisarski
Senior Scientist, Brookhaven National Laboratory

Dominik Schneble
Associate Professor, Department of Physics and Astronomy

This dissertation is accepted by the Graduate School.

Charles Taber
Interim Dean of the Graduate School

Abstract of the Dissertation
Holographic Pomeron

by

Alexander Stoffers

Doctor of Philosophy

in

Physics

Stony Brook University

2013

This thesis discusses the approach to hadronic scattering at high energies and the description of the pomeron within holographic QCD.

Based on a stringy Schwinger mechanism in curved space, the pomeron emerges through the exchange of closed strings between two dipoles and yields Regge behavior for the elastic scattering amplitude. At low momentum transfer, the holographic space is approximately flat and the string propagator which governs the pomeron dynamics obeys a diffusion equation in rapidity and impact parameter space. This diffusive process at strong coupling in holography connects to the early idea of Gribov (parton) diffusion in QCD at strong coupling. Curvature corrections to the flat-space scattering amplitude in a confining background define the wee-dipole density after identifying the holographic coordinate with the

inverse virtuality of the dipoles. The curvature corrected pomeron intercept is compared to the phenomenological value. The exponentiated 1-pomeron exchange amplitude saturates and we give an explicit derivation of the dipole saturation momentum both in the conformal and confining background. Our holographic result for the dipole-dipole cross section and the wee-dipole density in the conformal limit are shown to be identical in form to the BFKL pomeron result when the non-critical string transverse dimension is $D_{\perp} = 3$. Thus, we have obtained an evolution for the wee-dipole density as a function of both rapidity, impact parameter *and* virtuality.

The open string picture allows us to define a local Unruh temperature associated with the scattering process, which is small as the impact parameter is large and small compared to the Hagedorn temperature. Associated with the temperature on the boundary, the Unruh temperature allows us to define the free energy of the system. The induced instanton on the string world-sheet carries entropy for a dipole source of N-ality k . This stringy entropy is neither coherent nor thermal. We argue that it is released promptly over a time that is solely determined by the impact parameter and the rapidity. It may explain the 3/2 jump in the total charged multiplicities at about 10 participants reported over a wide range of collider energies by PHOBOS. We predict the charged multiplicities in pp , pA and central AA collisions at LHC. The total dipole-dipole cross section is compared to DIS data from HERA and the holographic result for the differential cross section compared to proton-proton and deeply virtual Compton scattering data. With the holographic parameters close to QCD expectations, the holographic results are in reasonable agreement with the data for a variety of observables in the Regge regime.

Contents

Acknowledgements	vii
1 Introduction	1
2 High energy hadronic scattering	8
2.1 Regge regime	9
2.2 Pomeron	12
2.3 Overview of approaches	14
2.3.1 Dipole-dipole scattering in QCD	14
2.3.2 Scattering in holographic QCD, AdS/CFT	14
3 Holographic pomeron	17
3.1 Dipole-dipole scattering	19
3.2 Wilson loop correlator	25
3.3 Scattering amplitude, cross section and the Froissart bound	28
3.4 Gribov Diffusion	30
3.4.1 Conformal	33
3.4.2 Confining	35
3.4.3 Wee-Dipole Density	37
3.5 Saturation	40
3.5.1 Conformal	45
3.5.2 Confining	47
3.6 Stringy Instanton	49
3.7 Schwinger mechanism and Unruh phenomenon	51
3.8 Entropy	53

3.9	Formation time	55
4	Comparison to experiment	56
4.1	Deep inelastic scattering	57
4.2	Diffractive pp scattering	62
4.2.1	Comparison to data: ISR	62
4.2.2	Comparison to data: LHC	66
4.3	Deeply virtual Compton scattering (DVCS)	67
4.4	Multiplicities	69
5	Conclusion	74
	Bibliography	77

Acknowledgements

First and foremost, I would like to thank my advisor Ismail Zahed. I have enjoyed learning from an inspiring teacher and working with a great mentor. Thanks to the nuclear theory faculty, Edward Shuryak, Derek Teaney, Dmitri Kharzeev, Jacobus Verbaarschot and Thomas Kuo for creating such a stimulating atmosphere.

Thanks to the members of my defense committee, Matthew Dawber, Robert Pisarski and Dominik Schneble.

A warm 'thank you' goes to the office crew, Frasher Loshaj, Pilar Staig, Tin Sulejmanpasic and Savvas Zafeiropoulos.

Thanks to Rafael Lopes de Sa and Adrien Poissier for vibrant discussion within and beyond the world of science.

I am in debt to Katelin Childers for proofreading this manuscript - thank you! Thanks to my family for their loving support.

Chapter 1

Introduction

The field of theoretical high energy hadronic scattering has a long and colorful history all in an effort to explain the experimental result that the total hadronic cross section slowly rises with the collision energy.

In the sixties, long before a field theoretical model for the strong interaction was developed, early attempts to describe the soft (low momentum transfer) hadronic interactions were done using Regge theory. However, the Regge trajectories of the known spectrum of particles did not lead to a rising cross section. Pomeranchuk and others [1–3] noticed that charge conjugation properties of the scattering objects get washed out at very high energies. Consequently, hadron-hadron and hadron-antihadron collisions will asymptotically have the same total cross section. The phenomenological approach to describe the data introduces a Regge trajectory with intercept close to one. Its lowest lying state is called the pomeron.

With the emergence of QCD in the seventies, an early field theoretic description of the pomeron was undertaken by Low [4] and Nussinov [5]. Even at high energies and moderate (strong and running) coupling, the perturbative gluon contributions to the scattering amplitude have to be resummed. This approach of reggeized gluons, pioneered by Balitsky, Fadin, Kuraev and Lipatov (BFKL) [6–8], is successful in describing hard scattering processes.

With the advent of perturbative QCD (pQCD), the unitarity problem at weak coupling surfaced. As a cure, the picture of parton saturation [9, 10] was in-

vented in the eighties. As the running coupling gets weak at high energies, the parton density becomes large and a semi-classical analysis known as Color Glass Condensate [11–14] can be applied.

A connection between the hard and soft scattering processes was sought after to study Regge properties of QCD with the HERA data available since the nineties. How to get to the soft pomeron from pQCD is still elusive and hints that an essentially non-perturbative approach is needed to describe the soft scattering regime.

With the gauge/gravity duality established in the late nineties came the possibility to access dynamical properties of a strongly coupled field theory. At the core of the duality is the description of a strongly coupled field theory with large gauge degrees of freedom through the means of weakly coupled gravity in higher, curved dimensions. It is this framework that we will use here to study hadronic interactions in the Regge regime.

The gauge/gravity duality or AdS/CFT correspondence [15, 16] suggests that large N gauge theories at strong coupling can be mapped onto weakly coupled gravity in higher dimensions. The strict form of the duality implies a conformal field theory on the boundary. We allow for deviations from the conformal regime and access the confining regime of the field theory by deforming the bulk gravity solution in order to describe a field theory closer to QCD. This approach is understood as holographic QCD. Early developments are found in [17, 18].

Knowing that soft hadronic scattering needs an essentially non-perturbative approach, holographic QCD gives us the possibility to describe strongly coupled dynamics analytically. We further know that the hard scattering QCD amplitude at high energies is dominated by a resummed gluon ladder exchange. The holographic setup describing a large N theory not only has the right degrees of freedom, but diagrammatically speaking, the gluon ladder resembles a surface which is readily at hand in the dual description as a string world sheet. It is now interesting to try to connect the hard and soft regime in a dual, holographic approach. The approach taken in this thesis further provides a qualitative understanding of saturation towards the strong coupling region.

Originally, elastic and inelastic parton-parton and dipole-dipole scattering in the pomeron limit were addressed using non-critical and variational surface exchanges in conformal and non-conformal AdS backgrounds [19–23]. The pomeron and reggeon emerge from an imaginary contribution to the Nambu-Goto string action in confined AdS with an unexplained multi-branch structure. Recently, key aspects of the pomeron were shown to follow from a stringy Schwinger mechanism in dipole-dipole scattering with different pomeron parameters [24]. The unexplained multi-branch structure observed in [21–23] follows from the N-ality of the dipole source.

An alternative derivation of the pomeron as a graviton using the Virasoro-Shapiro amplitude in 10 dimensions was suggested in [25–29]. While the amplitude is real in flat space, it was argued that the effect of curvature will cause it to reggeize with the spin-2 graviton transmuting to a spin-2 glueball Regge trajectory and the pomeron. While the surface exchange and the graviton approaches for the strongly coupled pomeron are similar in spirit, they differ in content. Indeed, in conformal AdS the multigraviton interactions are dominant for small dipoles [20], while in confined AdS gravitons are massive on distance scales of the order of the confinement scale where the dipole-dipole interaction is dominated by massless string exchange [24]. In the conformal limit, both approaches appear similar although with totally different parameters for the pomeron as the underlying exchange is different.

In perturbative QCD, dipole-dipole as onium-onium scattering has long been used to describe high energy scattering, [30–41]. In the 1-pomeron exchange, this is equivalent to the BFKL approach [6–8]. The scattering amplitude can be defined through the convolution of densities of the wee-dipoles originating from the parent dipoles and diffusing along the rapidity direction in transverse space. This fundamental diffusion was foreseen long ago by Gribov [42] and will be referred to as Gribov’s diffusion.

Diffractive dipole-dipole scattering in holographic QCD is dominated by

closed string pair creation at large rapidity χ and impact parameter \mathbf{b}_\perp . In [24] it was argued that the elastic and forward part of the dipole-dipole scattering amplitude is totally dominated by a string pair creation process reminiscent of the Schwinger particle pair creation process whereby the induced longitudinal electric field on the exchanged string worldsheet with string tension σ_T is $E/\sigma_T = \tanh(\chi/2)$. This induced electric field causes the string to feel a longitudinal acceleration and consequently a local Unruh temperature. The latter is an alternate and novel way of physically justifying Gribov’s wee parton diffusion in the context of the pomeron exchange. Thus, the scattering amplitude in holography is closely related to Gribov diffusion in curved space.

For a large impact parameter, the Unruh temperature is low and only the tachyon mode of the non-critical string is excited. This tachyonic string mode is diffusive in curved AdS_3 , which is reminiscent of Gribov’s diffusion in QCD. In particular, the properly normalized diffusion kernel with suitable boundary conditions in the infrared yields a wee-dipole density that is similar to the QCD one in the conformal limit. The convolution of the two wee-dipole densities yields the eikonalized scattering amplitude and allows for a “partonic” picture similar to [43, 44], albeit at strong coupling.

Diffusion means dynamics without bulk motion and can either be addressed in a phenomenological approach as a gradient expansion (Fick’s law) or on a fundamental level as a random walk of its microstates. In our approach, the connection between the two is the following: the expansion in curvature corrections to the amplitude allows us to define a wee-dipole density on the boundary, whose source in bulk is randomly walking string.

As the analysis of the Schwinger mechanism in [24] was carried out using string exchange at low momentum transfer in the flat space approximation, it is important to extend it to curved AdS space. Below, we show that the extension to conformal AdS_3 (short for transverse AdS_5) yields a result that is similar to the one for the onium-onium scattering amplitude following from the BFKL pomeron exchange in QCD, the differences being the pomeron intercept and diffusion constant. We also discuss the concept of dipole saturation for a conformal and confining AdS_3 background, a point of intense interest both at

HERA and present and future colliders.

In [21–24] it was suggested that in the pomeron regime with confining geometry, the string is far from critical and supersymmetric with $D_{\perp} < 8$. The QCD gluon ladder exchange is conformal at weak coupling, so it is natural to enforce conformality on the string exchange. As we will show below this is naturally achieved by extending the string in the holographic direction in $D_{\perp} = 3$ with hyperbolic or AdS curvature.

The ensuing wee-dipole distribution and cross sections in our approach at strong coupling compare favorably with those obtained using the BFKL resummation kernel at weak coupling. The holographic pomeron in $D_{\perp} = 3$ follows from an effective string theory perhaps of the type advocated by Luscher [45]. While we will use holographic QCD in the form of AdS₅ with a hard wall as a model throughout, a more systematic approach within holography and following Luscher’s long string arguments may be sought in AdS along the arguments in [46].

The holographic, strong coupling description allows access to the saturation regime at small Bjorken x and small momentum transfer and we compare the holographic dipole-dipole cross section to DIS data from HERA. This leads to a fit of the t’Hooft coupling λ through the slope of the proton structure function F_2 , while the remaining parameters are adjusted to be in reasonable agreement with QCD expectations. In the kinematical regime present at HERA, both contributions are of the same order of magnitude and a fit of the parameters shows the necessity for a confining geometry.

Exclusive diffractive processes such as proton-proton (pp) diffraction and deeply virtual Compton scattering (DVCS) reveal information about the proton shape in the transverse plane. The holographic dipole-dipole scattering model is used to describe pp diffraction and DVCS. At large momentum transfer, the holographic differential pp cross section is sensitive to length scales of the typical string length which in the confining background is of the order of

the IR cutoff. To get a better fit on the two parameters concerning the effective size of the proton and the IR cutoff, we compare the holographic result for diffractive proton-proton and DVCS cross sections with the data. Other attempts to use the gauge/gravity duality to describe pp diffraction and DVCS can be found in [47, 48] and [49–52].

The issue of how entropy is released in hadron-hadron and nucleus-nucleus collisions is a fundamental problem in the current heavy-ion program at collider energies. How coherence, which is a hallmark of a fundamental collision, turns to incoherence, which is at the origin of the concept of entropy, is a theoretical question of central importance. A possible understanding of the entropy deposition was attempted at weak coupling through the concept of the color glass approach in classical but perturbative QCD [53–55] and at strong coupling through the concept of black hole formation in holographic QCD [56–60].

The evidence of a strongly coupled plasma released at collider energies with large and prompt entropy deposition and flow suggest that a strong coupling approach is needed for the mechanism of entropy decomposition. In this way, the holographic approach with the release of a black hole falling along the holographic direction provides a plausible mechanism for entropy production. However, this mechanism is detached from our understanding of fundamental pp collisions, which are after all the seeds at the origin of the entropy production. Here we present an attempt to provide such an understanding.

This thesis is based on the following publications in collaboration with my advisor Ismail Zahed.

- “Holographic Pomeron and Entropy” arXiv:1211.3077, submitted to Phys. Rev. D
- “Diffractive and deeply virtual Compton scattering in holographic QCD” arXiv:1210.3724, published in Acta Phys.Polon.Supp. 6 (2013) 7-12,
- “Holographic Pomeron: Saturation and DIS” arXiv:1205.3223, published in Phys. Rev. D 87, 075023 (2013)

My other articles published during my PhD studies at Stony Brook are

- “Jet quenching in shock waves” with Ismail Zahed and Michael Spillane, arXiv:1110.5069, published in JHEP 1202, 023 (2012)
- “Holographic Jets in an Expanding Plasma” with Ismail Zahed, arXiv:1110.2943, published in Phys. Rev. C 86, 054905 (2012)
- “ $\gamma^*\gamma^* \rightarrow \pi^0$ Form Factor from AdS/QCD” with Ismail Zahed, arXiv:1104.2081, published in Phys. Rev. C 84, 025202 (2011)
- “Improved AdS/QCD Model with Matter” with Ismail Zahed, arXiv:1009.4428, published in Phys. Rev. D 83, 055016 (2011)

Chapter 2

High energy hadronic scattering

In this chapter, we introduce the scattering amplitude in the high energy (Regge) regime. The energy scaling is characterized by Regge trajectories. The scattering amplitude is related via the optical theorem to the total cross section and is dominated by the lowest lying Regge trajectory, the pomeron. We will give a brief overview of the different approaches towards dipole-dipole scattering in QCD and the formulation of high energy scattering in gauge/gravity duality.

Experiments on high energy hadronic scattering with small momentum transfer show a striking feature: the cross section slowly rises with the energy. Theoretically this imposes a challenge. A description of the scattering process through an exchange of known particles fails to describe the data. One approach is to introduce Regge trajectories. The spectrum of known particles seems to relate the mass m to the spin j as $m^2(j) \sim j$, see Figure 2.1. More generally, we can describe the scattering amplitude through reggeon exchange, characterized by the Regge trajectory $\alpha(t)$. For soft processes, the trajectory is characterized by the intercept and the slope.

2.1 Regge regime

The phenomenology of soft high energy scattering reduces the scattering problem to the exchange of reggeons. The family of reggeons corresponds to poles in the complex angular momentum plane of the scattering amplitude. The scattering process is captured by the the S -matrix, which translates the initial to the final states,

$$\mathbf{S}_{fi} = \delta_{fi} + i(2\pi)^4 \delta^4(p_f - p_i) \mathbf{T}_{fi} , \quad (2.1)$$

where $p_{f,i}$ represent the sum of the final and initial momenta respectively. The transfer or T -matrix is defined through the unitarity of the S -matrix and its elements relate to the total cross section as

$$Im T_{fi} = s \sigma_{fi}^{tot} . \quad (2.2)$$

For the case of elastic scattering of two particles with incoming momenta p_1, p_2 and outgoing momenta p_3, p_4 , the Mandelstam variables are defined as $s = (p_1 + p_2)^2 = (p_3 + p_4)^2$ and $t = (p_1 - p_3)^2 = (p_2 - p_4)^2$. A partial wave expansion for the T -matrix in the t -channel with $\cos \theta = 1 + 2s/t$ reads

$$T_{fi}(s, t) = \sum_{l=0}^{\infty} (2l+1) a_l(t) P_l(\cos \theta) . \quad (2.3)$$

Physical bound states are poles in the partial wave amplitude $a_l(k)$. The sum is changed into a complex integral, integrating over a contour \mathcal{C} including the real positive axis. Then the spin l is treated as a complex variable and Regge trajectories are defined through $a_l(k) \rightarrow a(l, k)$.

In order to be able to close the contour on the imaginary axis, we have to introduce a signature factor η . Eq. (2.3) can be rewritten as

$$T_{fi}(s, t) = \frac{1}{2i} \int_{\mathcal{C}} dl \frac{2l+1}{\sin l\pi} \sum_{\eta=\pm 1} \frac{\eta + e^{i\pi l}}{2} a^\eta(l, t) P_l(\cos \theta) . \quad (2.4)$$

The (Regge) poles on the real positive axis yield the physical states. In the so

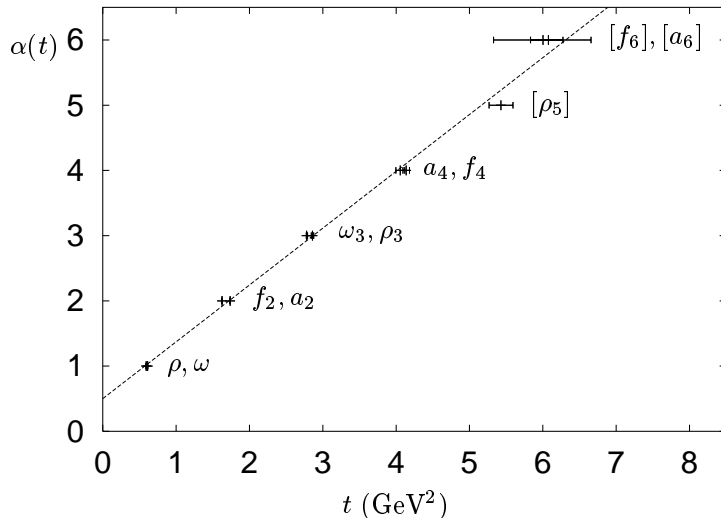


Figure 2.1: Chew-Frautschi plot from [61]. See text.

called Regge regime with $s \gg -t \gg m^2$, the asymptotics of P_l give

$$T_{fi} \sim \frac{\eta + e^{i\pi\alpha(t)}}{2 \sin(\pi\alpha(t))} \frac{s^{\alpha(t)}}{\Gamma(\alpha(t))}. \quad (2.5)$$

The cross section is dominated by the highest trajectory $\alpha(t)$. In the Regge regime, the trajectory is defined through the intercept $\alpha(0)$ and the slope α' as

$$\alpha(t) = \alpha_{\text{reggeon}} + \alpha' t. \quad (2.6)$$

The physical interpretation of the Regge trajectory $\alpha(t)$ for $-t = m^2$ is that of the spin j of the particle. This is illustrated for the meson spectrum in Figure 2.1, where the meson masses are plotted against the spin. The trajectory appears linear and can be fitted with $\alpha_{\text{meson}}(0) = 0.55$ and $\alpha' = 0.86 \text{ GeV}^{-2}$. The total cross section (2.2) has an asymptotic high energy behavior that is

governed by the Regge trajectory (2.6)

$$\sigma_{tot}(s) \sim s^{\alpha_{reggeon}-1} . \quad (2.7)$$

Describing the interaction by massless spin zero scalar exchange yields $\sigma_{tot} \sim s^{-1}$. Massless spin one vector exchange yields $\sigma_{tot} \sim s^0$ and exchanging spin two objects leads to a rising cross section $\sigma_{tot} \sim s^1$.

2.2 Pomeron

Pomeranchuk [1, 2] noted that any scattering process mediated by charged particles vanishes at asymptotically high energies. Conversely, Foldy and Peierls [3] found that when a cross section does not vanish asymptotically, it must be dominated by the exchange of vacuum quantum numbers. In order to describe the experimental data which show a slowly rising hadronic cross section, $\sigma_{tot} \sim s^{0.08 \div 0.4}$, a Regge trajectory with intercept slightly larger than one, (2.7), that has vacuum quantum numbers is needed. This trajectory is called the pomeron.

The measured cross sections on hadronic scattering offers the ability to distinguish two kinematical regimes. The soft pomeron regime with $-t > 0$ and the hard pomeron regime with $-t < 0$.

The soft regime is dominated by IR dynamics and needs an essentially non-perturbative description. We can think of the exchange as being mediated by glueballs of mass $\sqrt{-t}$ and spin $\alpha_{\mathbf{P}}(t)$. The pomeron trajectory is given by $\alpha_{\mathbf{P}_{soft}}(t) \simeq 1.08 - (0.25 \text{ GeV}^{-2})t$.

At sufficiently high energies the hard pomeron with $\alpha_{\mathbf{P}_{hard}} \simeq 1.4$ dominates the cross section. It is this UV regime where pQCD approaches are useful. The connection between the soft and hard pomeron is still elusive.

The approach taken here is using the gauge/gravity duality or holographic QCD to tackle the problem of hadronic scattering. Although no exact dual to QCD is known, the underlying field theory described is essentially strongly coupled and its dynamics are dominated by gauge fields. The pomeron exchange is described by string exchange in bulk. The lowest lying string mode, which is tachyonic, dominates the scattering amplitude and is identified with the pomeron. The string is bosonic and non-critical with transverse modes in three dimensional impact parameter space. In the Regge regime, the slice of the bulk space in which the string is propagating is approximately flat. Curvature corrections will modify the effective spin and the propagator of the pomeron. The pomeron described here is non-critical, meaning that the string

is long and not highly excited. The explosive pomeron is discussed in [62]. Exponentiating the 1-pomeron exchange allows us to drive the cross section towards the saturation regime, defining a density of “partons” in the scatterers at strong coupling.

2.3 Overview of approaches

2.3.1 Dipole-dipole scattering in QCD

QCD dipole-dipole scattering at large rapidity χ and weak coupling has been extensively discussed by Mueller and others [30–40]. This approach to high-energy hadron-hadron scattering was pioneered by Gribov [42, 63]. Typically, the scattering is viewed as a parent dipole of size a depleting into a cascade of daughter dipoles (wee-dipoles) and smashing against a similar parent dipole of size a' for fixed impact parameter \mathbf{b}_\perp . The onium-onium cross section in the 1-pomeron BFKL exchange reads [31]

$$\sigma_{\text{tot}}^{\text{BKFL}}(\chi) = 2\pi \frac{\lambda^{3/2}}{N_c^2} aa' \frac{e^{(\alpha^{\text{BKFL}}-1)\chi}}{(4\pi \mathbf{D}^{\text{BKFL}} \chi)^{1/2}}, \quad (2.8)$$

with

$$\begin{aligned} \alpha^{\text{BKFL}} &= 1 + \frac{\lambda}{\pi^2} \ln 2 \\ \mathbf{D}^{\text{BKFL}} &= 7\lambda\zeta(3)/(8\pi^2) \end{aligned} \quad (2.9)$$

the BFKL intercept and diffusion constant respectively. ζ is the Riemann zeta function and $\lambda = g^2 N_c$. The intercept can be understood as a perturbative series in λ at weak coupling.

2.3.2 Scattering in holographic QCD, AdS/CFT

Within the gauge/gravity duality, hadron-hadron scattering and the holographic pomeron has been discussed in numerous places, see e.g. [19–28, 64–71].

The AdS/CFT correspondence has allowed us to approach problems in field theories similar to QCD at strong coupling. Within this context, there are two approaches to tackle the problem of high energy scattering:

1. Scattering as an exchange of a classical surface as pioneered in [19, 20].

2. Exchange of closed string (or other SUGRA fields) in critical $D = 10$ dimensions using the Virasoro-Shapiro string amplitude, see [27].

We will now briefly discuss the two approaches.

1. The weakly coupled bulk gravity is described by a classical string action. The scattering process is described by a minimal surface exchange in bulk. Finding minimal surfaces in curved space is notoriously hard. One major simplification comes from the observation that the dynamics of the gauge theory on the boundary are dictated by a surface near the confining boundary. In the Regge regime with $t \ll s$, this IR region of space is approximately flat. The scattering amplitude is determined through a saddle point approximation to the Euclidean path integral. For scattering heavy quarks, the boundary conditions to the surface are well approximated by Wilson lines/loops and the surface is helicoidal.

2. While in flat space the critical string scattering amplitude is real, the effect of curvature will cause it to reggeize with the spin-2 graviton transmuting to a spin-2 glueball. With $\lambda \rightarrow \infty$ and to lowest order in string coupling, the scattering amplitude is dominated by one-graviton exchange and the dual pomeron in curved space string theory is a closed string graviton. A confining geometry will induce a mass on the transverse fluctuations of the metric tensor. These fluctuations are identified with a glueball on the boundary. At finite λ , the pomeron intercept gets curvature corrections and reads $\alpha_{\mathbf{P}(graviton)} = 2 - 2/\lambda$.

While the surface exchange and the graviton approaches for the strongly coupled pomeron are similar in spirit, they differ in content. Indeed, in conformal AdS the multigraviton interactions are dominant for small dipoles [20], while in confined AdS gravitons are massive on distance scales of the order of the confinement scale where the dipole-dipole interaction is dominated by massless string exchange [24]. In the conformal limit, both approaches appear similar although with completely different parameters for the pomeron as the

underlying exchange is different.

Chapter 3

Holographic pomeron

In this chapter, we will introduce the setup to the problem of hadronic scattering in holographic QCD through dipole-dipole scattering. The scattering amplitude is formulated in Euclidean space, where the two dipoles, represented by Wilson loops, are sloped at an angle θ which translates to a rapidity gap χ when analytically continued to Minkowski space. The two loops are separated by an impact parameter \mathbf{b}_\perp . The Wilson loop correlator gives the scattering amplitude and is calculated for the exchange of long, non-critical strings in a slice of AdS_5 , which we first approximate as flat. The longitudinal string modes generate the pole structure of the correlator while the transverse modes contribute to the diffusive properties of the string propagator. The loop-loop correlator is dominated by the lowest lying tachyonic string mode. We will show that the resulting cross section saturates the Froissart bound.

The diffusive nature of the propagator is used to include curvature corrections to the amplitude and allows for the definition of a wee-dipole density in a confined background. This density compares to the BFKL result in the UV regime. With the dipole density at hand, we will then proceed to describe the saturation regime in our holographic setup. We study the parameter dependence of the saturation momentum and compare it to phenomenological QCD approaches.

The Schwinger pair production mechanism used here relies on an electric field in the T-dual description of the open string. We briefly review the connection

between the Schwinger mechanism and the Unruh effect. The electric field stems from the longitudinal string modes and its acceleration induces an Unruh temperature on the string world-sheet. The string action equates to a free energy and with the Unruh temperature as the local temperature of the field theory at hand we can identify an entropy associated to the entropy process. This entropy when expressed in the dynamical degrees of freedom, i.e. the wee-dipoles, reveals that the ensemble here is neither thermal nor coherent. Describing the entropy produced in the prompt stage of a collision, we can identify the time it takes for the entropy to be released.

3.1 Dipole-dipole scattering

The color dipole approach is useful to address the problem of high energy scattering. Since the pomeron is an object with vacuum quantum numbers, the color dipole has the correct degrees of freedom. It allows to connect the quantum mechanical diffraction process to QCD.

We will now set up the basic formulation for the elastic dipole-dipole scattering amplitude [72–75]. The dipoles are described by Wilson loops and we seek to express the scattering amplitude in terms of the two loop correlator. The dynamics are imposed by the impact parameter \mathbf{b}_\perp , conjugate to the transferred momentum \mathbf{q}_\perp and the rapidity gap χ related to the collisional energy. We will then use the formulation of the Wilson loop expectation value in a holographic setup to compute the scattering amplitude.

We recall the scattering-, or S-matrix (2.1), which carries all information about the scattering of the initial to the final state, being defined as

$$\mathbf{S}_{fi} = \delta_{fi} + i(2\pi)^4 \delta^4(p_f - p_i) \mathbf{T}_{fi} , \quad (3.1)$$

where $p_{f,i}$ are the sum of the final and initial momenta. At high energies, the eikonal approximation results in the factorization of the T-matrix and the matrix elements, i.e. the scattering amplitudes, can be expressed as [73, 76, 77]

$$\mathcal{T}_{12 \rightarrow 34}(s, \mathbf{q}_\perp) = 2is \int du_1 du_2 \psi_4(u_1) \psi_3(u_1) \mathcal{T}_{DD}(\chi, \mathbf{q}_\perp, u_1, u_2) \psi_2(u_2) \psi_1(u_2) \quad (3.2)$$

where u_i is related to the transverse size of the dipole element described by the wave function ψ_i . The dipole-dipole scattering amplitude is given by

$$\mathcal{T}_{DD}(\chi, \mathbf{q}_\perp, u_1, u_2) = \int d^{D_\perp} \mathbf{b}_\perp e^{i\mathbf{q}_\perp \cdot \mathbf{b}_\perp} (1 - \langle \mathbf{W}(C_1) \mathbf{W}(C_2) \rangle_G) \quad (3.3)$$

$$\equiv \int d^{D_\perp} \mathbf{b}_\perp e^{i\mathbf{q}_\perp \cdot \mathbf{b}_\perp} \mathbf{W} \mathbf{W} , \quad (3.4)$$

where the integration is taken over the D_\perp dimensional impact parameter space separating the two dipoles. We will adapt the normalization $\langle \mathbf{W} \rangle = 1$ and focus only on the connected part of the correlator. The subscript G indicates that

the expectation value of the Wilson loop correlator is taken over gauge fields. In QCD this implies that the gluonic flux tube does not break by dynamical quark-, antiquark pair-production. The Wilson loops are evaluated along the surfaces C_1, C_2 . Note that in the eikonal approximation, the ultrarelativistic dipole constituent is a scalar since it moves nearly on the light cone. In (3.3) we have suppressed a dependence on the individual parton momenta and the total momentum of the dipole is equally distributed amongst its components. The size of the dipole is largest when the momentum is unequally distributed and, hence, we are restricting our analysis to small dipoles [78].

In QCD with massive quarks, each Wilson loop represents a quark-anti-quark dipole [79, 80] and is defined as

$$\mathbf{W}(C) = \frac{1}{N_c} \text{tr} \left[P e^{-ig \oint dx^\mu A_\mu^a t^a} \right], \quad (3.5)$$

with the trace evaluated over the color degrees of freedom generated by the $SU(N_c)$ gauge group generators t^a which interact with the strong coupling g . In a static setup, when two quarks are separated by a distance L , (3.5) yields the quark-(anti)quark potential $V(L)$

$$\langle \mathbf{W} \rangle \sim e^{-TV(L)}, \quad (3.6)$$

where the loop is rectangular in Euclidean space with sides $T \ll L$.

In a holographic setup with large N_c and large t'Hooft coupling λ the evaluation of the Wilson loop in the 4d field theory amounts to calculating a minimal surface in the bulk space with the appropriate boundary conditions [81, 82]. The Wilson loop is the minimal surface, spanned by a string ending on the boundary of the AdS space. Calculating the renormalized classical (gravity) action of the string gives the expectation value of the Wilson loop in the dual gauge theory. The endpoints of the string transform under the N_c of the gauge group $U(N_c)$. Their mass is inversely proportional to the distance from the endpoint to the boundary. Thus, a string with the two endpoints at the boundary can be interpreted as two very massive quarks in the

field theory and fluctuations of the world-sheet can be treated perturbatively [83, 84].

Early calculations of the Wilson loop correlator in static setup are found in [85–87]. The correlator between two circular loops is stable when the distance separating the loops is of the order of the radius of the individual loops. A Gross-Ooguri phase transition [86] occurs when the distance is much larger than the radius; in order to elongate the surface in bulk, supergravity interactions in bulk between the two lumps are needed. In a non-supersymmetric setup, the potential between two heavy mesons is generated by the exchange of a “scalarball” [88].

In order to access the scattering amplitude, the boundary conditions for the Wilson loops change from a static to a *dynamic setup*. In Euclidean space, this amounts to changing the angle θ to a non-zero value. This is illustrated in Figure 3.1. The role of the angle is played by the rapidity interval after analytic continuation. This will yield an additional contribution to the static potential, which will be attributed by an ‘intrinsic’ entropy in the elastic scattering amplitude.

The problem of finding a minimal surface to the dynamic setup has a long history. Early approaches [19] attempting to solve for a string world-sheet at constant time slices yield a reggeized amplitude at large s , but fail to describe inelastic processes and give a negative pomeron intercept. In [20], a first order perturbation in the bulk AdS fields is taken into account. The intercept is purely kinematic, i.e. equal to one for the case of the graviton, as compared to the QCD expectation $s^{4\alpha_s N \ln(2)/\pi}$.

In this work, we will consider the setup as depicted in Figure 3.1. The idea is the following: When the dipoles are small compared to the impact parameter and the rapidity is large, the surface connecting the two dipoles is highly twisted and can then be approximated by the world-sheet of a string with the appropriate boundary conditions, see Figure 3.2. The holographic coordinate scales the momenta of the dipoles [25]. Accordingly, the change in the holographic, curved coordinate (Δz) from one end of the string to the other is proportional to the momentum transfer between the dipoles. Thus, in the Regge regime with $\sqrt{s} \gg \sqrt{-t} = \mathbf{q}_\perp$, the string is exchanged in an

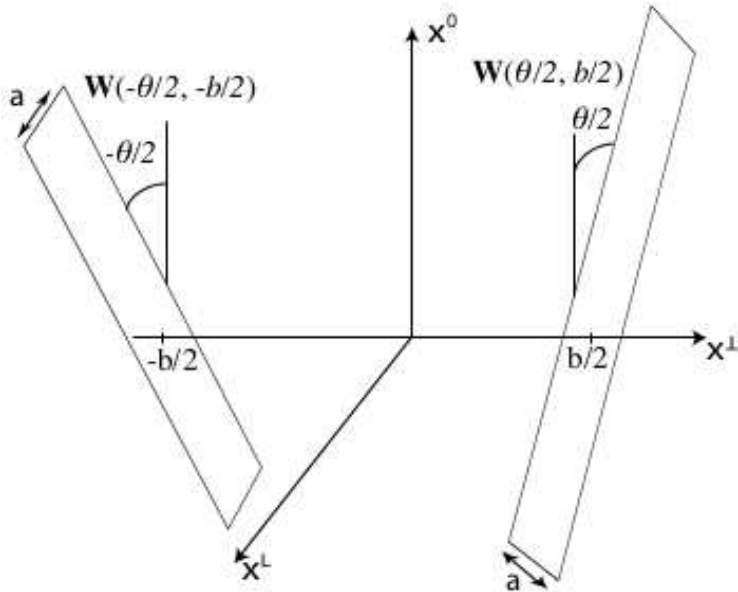


Figure 3.1: Dipole-dipole scattering setup in Euclidean space, see text. Figure from [24].

approximately flat background. To describe a scattering process in which a colorless object is exchanged, the string is bosonic and closed. We will neglect corrections to the tree level approximation as the string coupling will be assumed to be small. However, we will not limit ourselves to a classical string configuration but take into account (quantum) oscillations. A similar idea was put forward more than three decades ago [89].

The problem is set up in Euclidean space and then continued to Minkowski space. Due to the expected pole structure of the amplitude, the analytic continuation is by no means trivial. The degree of reliance of the continuation has been tested on the lattice [90, 91]. After analytic continuation from Euclidean to Minkowski space, the angle θ is transformed to the rapidity interval $\chi \equiv \chi_{max} + \chi_{min} = i\theta$, which is defined by

$$\cos \theta \rightarrow \cosh \chi \equiv \frac{1}{\sqrt{1-v^2}} = \frac{s}{s_0} - 1, \quad (3.7)$$

where the parameter s_0 is related to the effective transverse scattering mass

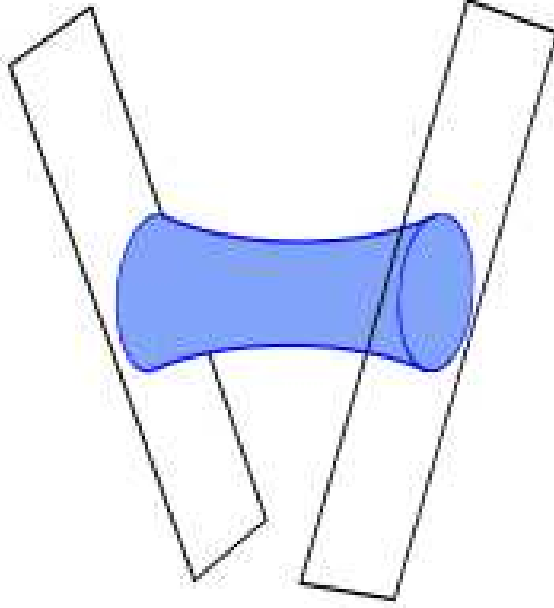


Figure 3.2: Twisted surface connecting the Wilson loops. See text. Figure from [24].

as $s_0 = m_\perp^2 = m^2 + p_\perp^2$.

As a background we will use $AdS_{D_\perp+2}$ with an IR cutoff realized through a hard wall at some z_0 . Although the field theory corresponding to this geometry is not exactly QCD, it captures essential features [44]. The space-time metric is Euclidean $AdS_{D_\perp+2}$

$$ds^2 = \frac{1}{z^2} \left((dx^0)^2 + (dx^L)^2 + (dx_\perp^1)^2 + \dots + (dx_\perp^{D_\perp-1})^2 + (dz)^2 \right) \quad (3.8)$$

where we have set the AdS radius to one. The IR cutoff is at some z_0 , i.e. $0 \leq z \leq z_0$. The dipoles of size a, a' are placed at the boundary $z = 0$.

The '1-loop' effective action yields the Wilson loop correlator

$$\mathbf{WW} = g_s^2 \int_0^\infty \frac{dT}{2T} \mathbf{K}(T) . \quad (3.9)$$

The closed string is parametrized by one parameter, the modulus ('circumference') T . The factor g_s^2 in (3.9) comes from the genus of the string configuration compared to the disconnected configuration. The string propagator reads

$$\mathbf{K}(T) = \int_T d[x] e^{-S[x]+ghosts} . \quad (3.10)$$

For closed, long strings with the interaction between the strings negligible, the effective string action is the Polyakov action

$$S = \frac{\sigma_T}{2} \int_0^T d\tau \int_0^1 d\sigma (\dot{x}^\mu \dot{x}_\mu + x'^\mu x'_\mu) \quad (3.11)$$

with $\dot{x} = \partial_\tau x$ and $x' = \partial_\sigma x$ and string tension σ_T . We have made the following gauge choice for the world-sheet metric $h_b^a = \delta_b^a$.

The string $x^\mu(\tau, \sigma)$ is closed

$$x^\mu(T, \sigma) = x^\mu(0, \sigma) \quad (3.12)$$

and attaches to the dipole surfaces

$$\cos(\theta/2)x^1(\tau, 0) + \sin(\theta/2)x^0(\tau, 0) = 0 \quad (3.13)$$

$$\cos(\theta/2)x^1(\tau, 1) - \sin(\theta/2)x^0(\tau, 1) = 0 . \quad (3.14)$$

We already see that the freedom in moving the intersection point of the string world-sheet with the dipole surfaces of width a , a' yields a factor aa' in the correlator, (3.9), (3.10).

3.2 Wilson loop correlator

The world-sheet is twisted in the x^0, x^1 coordinates

$$\begin{pmatrix} x^0 \\ x^1 \end{pmatrix} = \begin{pmatrix} \cos \theta_\sigma & -\sin \theta_\sigma \\ \sin \theta_\sigma & \cos \theta_\sigma \end{pmatrix} \begin{pmatrix} \tilde{x}^0 \\ \tilde{x}^1 \end{pmatrix} \quad (3.15)$$

with $\theta_\sigma = \theta(2\sigma - 1)$. This twist (rotation) in Euclidean space corresponds to a Lorentz boost in the longitudinal direction after analytic continuation.

We can now evaluate the Wilson loop correlator by solving for the bosonic string world-sheet with Neumann boundary conditions for \tilde{x}^0 and Dirichlet boundary conditions for \tilde{x}^1 . The Polyakov action is quadratic in the untwisted coordinates and the solutions can be parametrized as

$$\tilde{x}^0(\tau, \sigma) = \sum_{m=-\infty}^{+\infty} \sum_{n=0}^{+\infty} x_{mn}^0 e^{2\pi i m \tau / T} \cos(\pi n \sigma) \quad (3.16)$$

$$\tilde{x}^1(\tau, \sigma) = \sum_{m=-\infty}^{+\infty} \sum_{n=0}^{+\infty} x_{mn}^1 e^{2\pi i m \tau / T} \sin(\pi n \sigma) . \quad (3.17)$$

Note that the temporal component has a non-vanishing ground state similar to a zero mode

$$\tilde{x}_{ZM}^0(\tau, \sigma) \equiv \sum_{m=-\infty}^{+\infty} x_{m0}^0 e^{2\pi i m \tau / T} . \quad (3.18)$$

The transverse, untwisted coordinates are periodic with Dirichlet boundary conditions

$$x^\perp(\tau, \sigma) = -\mathbf{b}_\perp(1 - 2\sigma)/2 + \sum_{m=-\infty}^{+\infty} \sum_{n=0}^{+\infty} x_{mn}^\perp e^{2\pi i m \tau / T} \sin(\pi n \sigma) . \quad (3.19)$$

Since the action is quadratic, the propagator (3.10) factorizes as

$$\mathbf{K} = \mathbf{K}_{0L} \times \mathbf{K}_{\emptyset L} \times \mathbf{K}_\perp \times \mathbf{K}_{ghost} , \quad (3.20)$$

with the individual contributions \mathbf{K}_{0L} , $\mathbf{K}_{\emptyset L}$ from the longitudinal zero/non-zero modes, and \mathbf{K}_{\perp} the contribution from the \perp -modes. Due to the gauge choice for the string world-sheet metric, the propagator gets the ghost contribution \mathbf{K}_{ghost} .

The solutions are straight forward [24]. The contributions from the longitudinal modes reads

$$\mathbf{K}_{0L}(T) = (2 \sinh(\theta T/2))^{-1} \quad (3.21)$$

and

$$\mathbf{K}_{\emptyset L}(T) = \prod_{n=1}^{\infty} \prod_{s=\pm 1} (2 \sinh((n + s\theta/\pi)\pi T/2))^{-1} . \quad (3.22)$$

The transverse part of the propagator is given by

$$\mathbf{K}_{\perp} = e^{-\sigma \mathbf{b}_{\perp}^2 T/2} \eta^{-D_{\perp}}(iT/2) \quad (3.23)$$

with the Dedekind eta function

$$\eta(\tau) \equiv q^{1/24} \prod_n (1 - q^n) \quad (3.24)$$

and $q \equiv e^{2\pi i\tau}$. The ghost contribution to the propagator is given by

$$\mathbf{K}_{ghost}(T) = \prod_{n=1}^{\infty} 4 \sinh^2(n\pi T/2) . \quad (3.25)$$

We can now analytically continue from Euclidean to Minkowski space by letting $\theta \rightarrow -i\chi$. The loop-loop correlator then reads

$$\mathbf{W}\mathbf{W} = g_s^2 \int_0^{\infty} \frac{dT}{2T} \mathbf{K}(T) \quad (3.26)$$

$$= \frac{ig_s^2 aa'}{4\alpha'} \int_0^{\infty} \frac{dT}{T} \frac{1}{\sin(\chi T/2)}$$

$$\prod_{n=1}^{\infty} \prod_{s=\pm 1} \frac{\sinh(n\pi T/2)}{\sinh((n\pi + is\chi)T/2)} \eta^{-D_{\perp}}(iT/2) e^{-\mathbf{b}_{\perp}^2 T/4\pi\alpha'} . \quad (3.27)$$

For $\chi \rightarrow \infty$, we see that the longitudinal zero modes are responsible for the poles along the real T -axis. Picking up the residues at the positive poles $T = 2\pi k/\chi$, (3.27) equates to

$$\mathbf{W}\mathbf{W} = \frac{g_s^2 a a'}{4\alpha'} \sum_{k=1}^{k_{max}} \frac{(-1)^k}{k} \eta^{-D_\perp}(i\pi k/\chi) e^{-k\mathbf{b}_\perp^2/2\alpha'\chi} . \quad (3.28)$$

Using

$$\eta^{-D_\perp}(i\pi k/\chi) = \left(\frac{\pi k}{\chi}\right)^{D_\perp/2} e^{D_\perp\chi/12k} \prod_{n=1}^{\infty} (1 - e^{-2\chi n/k})^{-D_\perp} \quad (3.29)$$

$$= \left(\frac{\pi k}{\chi}\right)^{D_\perp/2} \sum_{n=0}^{\infty} d(n) e^{-2\chi n/k} , \quad (3.30)$$

we can rewrite the Wilson loop correlator as

$$\mathbf{W}\mathbf{W} = \frac{g_s^2 a a'}{4\alpha'} \sum_{k=1}^{k_{max}} \sum_{n=0}^{\infty} \frac{(-1)^k}{k} \left(\frac{\pi k}{\chi}\right)^{D_\perp/2} d(n) e^{-k\mathbf{b}_\perp^2/2\alpha'\chi + \chi D_\perp/12k - 2\chi n/k} . \quad (3.31)$$

For large n [92] the density of string state $d(n)$ rises exponentially

$$d(n) \sim \frac{e^{2\pi\sqrt{D_\perp n/6}}}{n^{D_\perp/4}} . \quad (3.32)$$

The correlator (3.28) is dominated by the lowest transverse mode, $n = 0$. The poles are at different winding k , which is interpreted as the N-ality. Since dipoles of representation k_{max} can only exchange strings of $k \leq k_{max}$, the sum over the N-ality is bounded. The action for a k -string is the same as overlapping k ($k = 1$)-strings. This is expected from large N QCD, where each source is screened by gluons. For long strings, the only information about the sources of the string that enters the Wilson loop is the N-ality [93]. We will now make a further connection to large N QCD with gauge group $SU(N_c)$ by considering only strings that are stable and thus have $k_{max} = [N_c/2]$, where $[N_c/2]$ is defined as $N_c/2$ if N_c even and $N_c/2 + 1/2$ if N_c odd. For QCD with $N_c = 3$, this limits the exchange to $k = 1, 2$ strings.

3.3 Scattering amplitude, cross section and the Froissart bound

The Froissart bound [94] gives the maximum scaling of the cross section allowed by unitarity (and analyticity) as

$$\sigma_{tot} \leq const. \ln^2 s \sim \chi^2 . \quad (3.33)$$

We will now show that the cross section (3.36) indeed saturates the Froissart bound.

Combining (3.4) and (3.28), the dipole-dipole scattering amplitude corresponding to 1-reggeon exchange reads

$$\begin{aligned} \mathcal{T}_{DD} = & 2is \int d^{D_\perp} \mathbf{b}_\perp e^{i\mathbf{q}_\perp \cdot \mathbf{b}_\perp} \frac{g_s^2 a a'}{4\alpha'} \\ & \sum_{k=1}^{k_{max}} \sum_{n=0}^{\infty} \frac{(-1)^k}{k} \left(\frac{\pi k}{\chi} \right)^{D_\perp/2} d(n) e^{-k\mathbf{b}_\perp^2/2\alpha'\chi + \chi D_\perp/12k - 2\chi n/k} . \end{aligned} \quad (3.34)$$

This is divergent as $s \rightarrow \infty$ and violates the unitarity bound on the S-matrix elements. Neglecting the reggeon-reggeon interaction, unitarity is restored by exponentiating the 1-reggeon exchange,

$$\mathcal{T}_{DD} = 2is \int d^{D_\perp} \mathbf{b}_\perp e^{i\mathbf{q}_\perp \cdot \mathbf{b}_\perp} (1 - e^{\mathbf{w}\mathbf{w}}) , \quad (3.35)$$

which yields via the optical theorem

$$\sigma_{tot}(s) = 2 \int d^{D_\perp} \mathbf{b}_\perp (1 - e^{\mathbf{w}\mathbf{w}}) . \quad (3.36)$$

For $s \rightarrow \infty$ the loop-loop correlator becomes negligible for $\mathbf{b}_\perp \geq \mathbf{b}_{max}$ and the cross section (3.33) is negligible for impact parameters larger than

$$\mathbf{b}_{max}^2 = \frac{D_\perp \alpha'}{6} \chi^2 . \quad (3.37)$$

In this regime, we expect the cross section to be dominated by the geometry

of the scatterers. At very high energies and impact parameters large enough to neglect the microscopic structure of the scatterers, we expect the dipoles to appear as 'black disks'. Indeed, (3.36) yields

$$\sigma_{tot}(s) \simeq 2 \int^{\mathbf{b}_{max}} d^{D_\perp} \mathbf{b}_\perp = 2\pi \mathbf{b}_{max}^2 = \frac{D_\perp \pi \alpha'}{3} \chi^2, \quad (3.38)$$

which nicely illustrates how the unitarization of the multi pomeron exchange saturates the Froissart bound (3.33) in $D_\perp = 2$.

3.4 Gribov Diffusion

Gribov diffusion [42, 95] reconciles the partonic picture with the non-perturbative aspects of hadronic interactions at high energies. The assumption is that hadronic interactions at strong coupling are the result of parton emission. Each emission changes the rapidity of the emitting parton, which results in a diffusive motion for the partons in impact parameter space. The difference in rapidities at the initial and following point in space mimics the diffusion time. The spread in impact parameter space results in a spread in momenta. The higher the energies, the 'broader' the diffusive regime and lower momenta start to become important. At large momentum, the hadron is Lorentz contracted and its effective volume grows with $\ln(s)$, compare (4.14), while the number of partons scales with the momentum as $s^\#$, compare (3.66). At higher and higher energies, the wave functions of the partons overlap and the probability to recombine balances the production. The scattering objects become 'black disks'. Gribov anticipated that this should result in a constant total cross section for *all* hadronic interactions.

We will now show that the string exchange picture naturally leads to a diffusive process reminiscent of Gribov diffusion in which the long string diffuses in rapidity through the impact parameter space. The diffusion constant will be related to the t'Hooft coupling λ . We will then motivate a wee-dipole density and show that it compares to the QCD BFKL expectation.

The Wilson loop correlator (3.31) and, hence, the scattering amplitude is dominated by the tachyonic $n = 0$ contribution. This $n = 0$ mode corresponds to the interacting pomeron. We can rewrite (3.28) as

$$\mathbf{W}\mathbf{W} \approx \frac{g_s^2}{4} \left(\frac{\pi}{\sigma_T} \right)^{D_\perp/2} \sum_{k=1}^{k_{max}} \frac{(-1)^k}{k} \frac{aa'}{\alpha'} \mathbf{K}_k(\chi, \mathbf{b}_\perp) . \quad (3.39)$$

The emerging propagator at the poles,

$$\mathbf{K}_k(\chi, \mathbf{b}_\perp) = \left(\frac{k}{2\pi\alpha' \chi} \right)^{D_\perp/2} e^{-k\mathbf{b}_\perp^2/2\chi\alpha' + D_\perp\chi/12k} \quad (3.40)$$

satisfies a diffusion equation in flat space

$$\left(\partial_\chi - \frac{D_\perp}{12k} \right) \mathbf{K}_k(\chi, \mathbf{b}_\perp) = \mathbf{D}_k \nabla_\perp^2 \mathbf{K}_k(\chi, \mathbf{b}_\perp), \quad (3.41)$$

with the diffusion constant $\mathbf{D}_k = \alpha'/2k$. The effects of curvature will become apparent at intermediate \mathbf{b}_\perp and are discussed below.

For long strings, the diffusion propagator (3.40) emerges as the natural version of the periodic string propagator in the diffusive regime $\mathbf{b}_\perp \sim \sqrt{\chi\alpha'}$. We note that (3.41) is just the proper time evolution of the tachyonic string mode

$$(\partial_{T_\perp} + (M_0^2 - \nabla_\perp^2)) \mathbf{K}_k(T_\perp, M, \mathbf{b}_\perp) = 0 \quad (3.42)$$

after the identification $T_\perp = \mathbf{D}_k\chi$. The tachyonic mass follows from the harmonic string spectrum

$$M_n^2 = \frac{4}{\alpha'} \left(n - \frac{D_\perp}{24} \right) \rightarrow -\frac{D_\perp}{6\alpha'}. \quad (3.43)$$

The occurrence of (3.42) is naturally explained by noting that the dominant contribution to the closed string propagator in (3.9) stems from short proper times $T_\perp = 2\pi k/\chi < 1$ [24]. We will show in section 3.7 that T_\perp is the period of the open string exchange by T-duality. So $T_\perp = 1/(\mathbf{b}_\perp T_U)$ effectively plays the role of a ‘temperature’ for the open string. Indeed explicit arguments in [24] show that $T_U \approx \chi/2\pi\mathbf{b}_\perp > 1$ acts as an Unruh temperature on the open string world-sheet after properly identifying the induced longitudinal electric field at the origin of this phenomenon. The Unruh temperature is high enough to yield a dimensional reduction of the open string from D to D_\perp dimensions. On the other hand, it is lower than the Hagedorn temperature for long and

non-critical strings and forces the the dominant string mode to be the ground state, the tachyon. Much like the heavy-quark string dimensionally reduces and diffuses at finite and real temperature [96], so does the holographic string under the effect of T_U . This analogy provides a physically novel interpretation of Gribov's wee parton diffusion [42] in the context of the pomeron exchange.

We now relax the condition of large $\mathbf{b}_\perp/\sqrt{\alpha'}$ and allow for curvature corrections on the \perp -modes. We focus on the dominant mode with N-ality $k = 1$, as higher order modes are exponentially suppressed. In our holographic setup, the curved coordinate z , compare (3.49), is inversely proportional to the momentum transfer \mathbf{q}_\perp . This allows us to evolve the scattering amplitude in the transferred momentum. However, no exact string solution to the equation of motion in AdS_5 is known. Although the exact form of the string propagator in curved AdS_5 space is unknown, we expect the longitudinal pole structure leading to the reduction (3.20) to remain unchanged since it follows from short proper times i.e. $T \sim 1/\chi < 1$, which are insensitive to curvature. On dimensional grounds, the diffusion constant will be the same as in the flat case. Since $\chi > 1$ we still expect a reduction of the tachyonic string to transverse space, which is curved on the diffusion time scale. Tachyon diffusion in curved space follows through

$$\left(\partial_{T_\perp} + (M_0^2 - \frac{1}{\sqrt{g_\perp}} \partial_\mu g_\perp^{\mu\nu} \sqrt{g_\perp} \partial_\nu) \right) \Delta_\perp(x_\perp, x'_\perp) = 0, \quad (3.44)$$

where we have suppressed T_\perp, M to alleviate the notation. The metric g_\perp in (3.44) is that of the transverse space with positive signature. Eq. (3.44) is the curved space generalization of (3.42). Below we show how the curved diffusion propagator Δ_\perp can be substituted for \mathbf{K}_k to generalize (3.39) to curved AdS . In general x_\perp is an arbitrary point in D_\perp . In hyperbolic AdS type spaces it is useful to separate $x_\perp = (\mathbf{x}, z)$ with z along the holographic direction and \mathbf{x} in the 2-dimensional physical space for $D_\perp = 3$ for instance with diffusion in AdS_3 . The formal solution to (3.44) reads

$$\Delta_\perp(x_\perp, x'_\perp) = \langle x_\perp | e^{-T_\perp(M_0^2 - \nabla_C^2)} | x'_\perp \rangle, \quad (3.45)$$

with $\nabla_{\mathcal{C}}^2$ the curved Laplacian in (3.44) and $T_{\perp} = \mathbf{D}\chi \gg 1$ for $k = 1$. The transverse evolution propagator Δ_{\perp} in (3.45) ties to the tachyon propagator $\mathbf{G}(j)$

$$\langle x_{\perp} | \mathbf{G}(j) \equiv (j + (M_0^2 - \nabla_{\mathcal{C}}^2))^{-1} | x'_{\perp} \rangle \quad (3.46)$$

through an inverse Mellin transform

$$\Delta_{\perp} = \int_{\mathcal{C}} \frac{dj}{2i\pi} e^{jT_{\perp}} \mathbf{G}(j) , \quad (3.47)$$

with \mathcal{C} a pertinent contour in the complex j -plane at the rightmost of all singularities. The tachyon propagator in (3.46) obeys the curved equation

$$(j + (M_0^2 - \nabla_{\mathcal{C}}^2)) \mathbf{G}(j, x_{\perp}, x'_{\perp}) = \frac{1}{\sqrt{g}} \delta_{D_{\perp}}(x_{\perp} - x'_{\perp}) . \quad (3.48)$$

A similar propagator was noted in [27] starting from the graviton using the critical closed string scattering amplitude in 10 dimensions.

3.4.1 Conformal

In transverse hyperbolic space $\text{AdS}_{D_{\perp}}$ with metric

$$ds^2 = \frac{1}{z^2} \left((dx_{\perp}^1)^2 + \dots + (dx_{\perp}^{D_{\perp}-1})^2 + (dz)^2 \right) \quad (3.49)$$

all length scales are measured in units of the AdS radius which is set to 1, and reinstated at the end by inspection. The propagator for a scalar field is given by [85, 97]

$$\mathbf{G}_{D_{\perp} \text{ odd}}(j, \xi) = \frac{1}{4\pi} \left(\frac{-1}{2\pi \sinh(\xi) \frac{d}{d\xi}} \right)^{m-1} \frac{e^{-\nu\xi}}{\sinh(\xi)} \quad (3.50)$$

for $D_\perp = 2m + 1$ and

$$\mathbf{G}_{D_\perp \text{ even}}(j, \xi) = \frac{1}{2\pi} \left(\frac{-1}{2\pi \sinh(\xi) \frac{d}{d\xi}} \right)^m \mathcal{Q}_{\nu-1/2}(\cosh(\xi)) \quad (3.51)$$

for $D_\perp = 2m$ with

$$\begin{aligned} \nu^2 &= j - j_0 \\ j_0 &= -M_0^2 - (D_\perp - 1)^2/4. \end{aligned} \quad (3.52)$$

\mathcal{Q} is a Legendre function of the second kind. The chordal distance ξ is defined through

$$\cosh \xi = 1 + d = 1 + \frac{\mathbf{b}_\perp^2 + (z - z')^2}{2zz'}, \quad (3.53)$$

which gives for $\frac{\mathbf{b}_\perp^2}{2zz'} \gg 1$

$$\xi \sim \ln \left(\frac{\mathbf{b}_\perp^2}{zz'} \right), \quad \sinh(\xi) \sim \frac{\mathbf{b}_\perp^2}{2zz'}. \quad (3.54)$$

For $D_\perp = 3$, inserting the conformal propagator (3.50) in (3.47) yields the conformal evolution kernel

$$\Delta_\perp(\chi, \xi) = \frac{e^{j_0 \mathbf{D} \chi}}{(4\pi \mathbf{D} \chi)^{3/2}} \frac{\xi e^{-\frac{\xi^2}{4\mathbf{D} \chi}}}{\sinh(\xi)}, \quad (3.55)$$

with the diffusion constant $\mathbf{D} = \alpha'/2 = 1/(2\sqrt{\lambda})$ for conformal AdS₃, after restricting the N-ality to $k = 1$. This heat kernel was obtained in [98] using a group theoretical approach. Equation (3.55) shows that in conformal AdS₃, the tachyon mode of the bosonic string diffuses in hyperbolic space along the chordal distance as measured by ξ^2 which is about twice the geometric distance for small displacement, i.e. $\xi^2 \approx 2d \ll 1$. Again the rapidity χ plays the role of time.

3.4.2 Confining

Confinement in AdS is captured in a simplified way by the hard-wall model, whereby only a slice of the AdS space is considered with $0 \leq z \leq z_0$ and $z_0 \approx 1/\Lambda$ setting up the confinement scale [26]. In this case, all scales are set by z_0 implicitly in the intermediate expressions and explicitly in the final ones. We note that in the hard wall model we still use the identification $\alpha' \equiv l_s^2/z_0^2 \equiv \sqrt{\lambda}$.

To simplify the analysis for the curved diffusion, we define the total wee-dipole density $\mathbf{N} = \Delta/(zz')^{D_\perp-2}$. Since the scattering amplitude is symmetric under the interchange of the two dipoles and we are going to identify z, z' with the effective size of the dipoles, the correct rescaling of \mathbf{N} is by powers of zz' . Using the conformal variable $u = -\ln(z/z_0)$, the diffusion equation for the dipole density reads

$$\left(\partial_{T_\perp} + (M_0^2 + D_\perp - 2) - \partial_u^2 - e^{2u} \nabla_{\mathbf{b}_\perp}^2 \right) \mathbf{N} = 0 . \quad (3.56)$$

The proper time evolution of \mathbf{N} in AdS amounts to a transport or diffusion equation with the initial condition

$$\mathbf{N}(T_\perp = 0, u, u', \mathbf{b}_\perp) = \delta(u - u') \delta(\mathbf{b}_\perp) \quad (3.57)$$

as one-dipole per unit area in the transverse \mathbf{b}_\perp .

The boundary condition for solving (3.56) follows from the conservation of the diffusion charge in the slab $0 \leq z \leq z_0$ or $0 \leq u \leq \infty$,

$$\frac{d}{dT_\perp} \int du d\mathbf{b}_\perp e^{T_\perp(M_0^2 + D_\perp - 2)} \mathbf{N} = \int d\mathbf{b}_\perp e^{T_\perp(M_0^2 + D_\perp - 2)} \partial_{u=0} \mathbf{N} , \quad (3.58)$$

assuming that the diffusion current vanishes at $\mathbf{b}_\perp = \infty$ and at $u = \infty$ (UV boundary) as no holographic source is subsumed. Thus, the Neumann boundary condition

$$\partial_{u=0}\mathbf{N} = 0 \tag{3.59}$$

enforces that the (singlet) wee-dipole current does not leak in the infrared at $z = z_0$. As a result

$$\int du d\mathbf{b}_\perp e^{T_\perp(M_0^2+D_\perp-2)} \mathbf{N} \equiv 1 \tag{3.60}$$

is fixed both in the conformal and confining case. Other boundary conditions on the wall, e.g. absorptive or mixed, will result in wee-dipole current loss in the infrared or confining region, with (3.60) less than 1.

The solution to (3.56) subject to (3.57-3.59) is readily obtained by the image method for the current conserving Neumann boundary condition

$$\mathbf{N}(T_\perp, u, u', \mathbf{b}_\perp) = \frac{1}{z_0^2} e^{u'+u} \Delta(\chi, \xi) + \frac{1}{z_0^2} e^{u'-u} \Delta(\chi, \xi_*) \tag{3.61}$$

$$= \frac{1}{zz'} \Delta(\chi, \xi) + \frac{z}{z'z_0^2} \Delta(\chi, \xi_*) , \tag{3.62}$$

with the conformal solution (3.55) for $\Delta(\chi, \xi)$. The invariance of the interchange of the two dipoles in the conformal case gets affected in the confining contribution (second part of (3.62)). The chordal distances follow from (3.53) as

$$\cosh\xi = \cosh(u' - u) + \frac{1}{2} \mathbf{b}_\perp^2 e^{u'+u} \tag{3.63}$$

$$\cosh\xi_* = \cosh(u' + u) + \frac{1}{2} \mathbf{b}_\perp^2 e^{u'-u} , \tag{3.64}$$

with $-u$ the image of u with respect to the holographic wall at $u = 0$.

3.4.3 Wee-Dipole Density

\mathbf{N} obeys a Markovian type chain rule

$$\begin{aligned} \int du'' d\mathbf{b}_\perp'' & \mathbf{N}(T_\perp - T_\perp'', u, u'', \mathbf{b}_\perp - \mathbf{b}_\perp'') \times \mathbf{N}(T_\perp'' - T_\perp', u'', u', \mathbf{b}_\perp'' - \mathbf{b}_\perp') \\ & = \mathbf{N}(T_\perp - T_\perp', u, u', \mathbf{b}_\perp - \mathbf{b}_\perp'), \end{aligned} \quad (3.65)$$

which follows readily from the diffusion evolution kernel as a propagator in rapidity space. Equation (3.65) suggests a Weizsaecker-Williams analogy for the virtual dipole field surrounding each of the initial projectile and target dipole. Thus, the total number of wee-dipoles either in the target or the projectile follows from the normalization

$$N_{wee} = \int du d\mathbf{b}_\perp \mathbf{N} = e^{-T_\perp(M_0^2 + D_\perp - 2)} \equiv (s/s_0)^{\alpha_{\mathbf{P}} - 1} \quad (3.66)$$

with the $1/\sqrt{\lambda}$ corrected intercept

$$\alpha_{\mathbf{P}} = 1 + \frac{D_\perp}{12} - \frac{(D_\perp - 1)^2}{8\sqrt{\lambda}} \quad (3.67)$$

for $D_\perp = 3$. \mathbf{N} is interpreted as the density of wee-dipoles of scale u at a transverse distance \mathbf{b}_\perp sourced by a dipole of scale u' located at $\mathbf{b}'_\perp = \mathbf{0}$. Their total number or multiplicity is given by (3.66) and grows exponentially with the rapidity. This growth is at the origin of the violation of unitarity in the scattering amplitude. Here it is tamed by the eikonized amplitude whereby a class of $1/N_c$ corrections are resummed.

Using the chain rule (3.65) and the dipole density (3.62), we obtain the asymptotic dipole density

$$\mathbf{N}(\chi, z, z', \mathbf{b}_\perp) \approx 2 \frac{e^{(\alpha_{\mathbf{P}} - 1)\chi}}{(4\pi \mathbf{D}\chi)^{3/2}} \frac{z}{z' \mathbf{b}_\perp^2} \ln \left(\frac{\mathbf{b}_\perp^2}{zz'} \right) e^{-\ln^2 \left(\frac{\mathbf{b}_\perp^2}{zz'} \right) / (4\mathbf{D}\chi)} \quad (3.68)$$

in the conformal case and in the limit $\frac{\mathbf{b}_\perp^2}{zz'} \gg 1$. The analogue of (3.68) in the

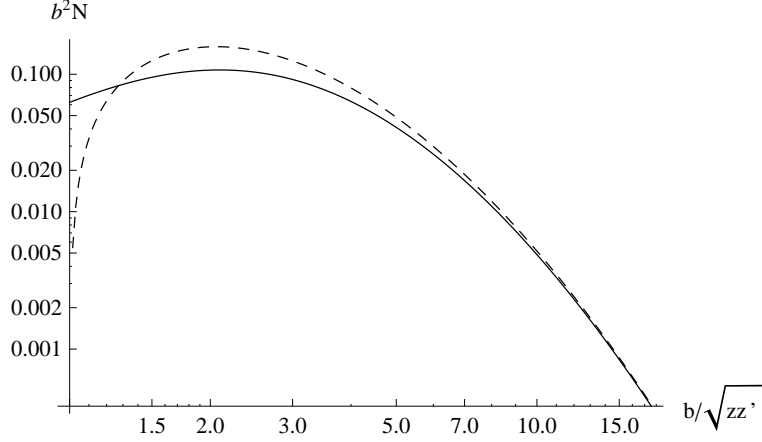


Figure 3.3: Holographic wee-dipole spatial distributions for $z = z' = 1.8 \text{ GeV}^{-1}$ and $\chi = 10$. Confining density in (3.62): solid curve; asymptotic density in (3.68): dashed curve. See text.

context of onium-onium scattering was discussed in [31–33]. In particular, in the BFKL 1-pomeron approximation it is given by [31]

$$\mathbf{N}^{\text{BFKL}}(\chi, z, z', \mathbf{b}_\perp) \approx 2 \frac{e^{(\alpha^{\text{BFKL}} - 1)\chi}}{(4\pi \mathbf{D}^{\text{BFKL}} \chi)^{3/2}} \frac{z}{z' \mathbf{b}_\perp^2} \ln \left(\frac{\mathbf{b}_\perp^2}{zz'} \right) e^{-\ln^2 \left(\frac{\mathbf{b}_\perp^2}{zz'} \right) / (4 \mathbf{D}^{\text{BFKL}} \chi)}, \quad (3.69)$$

with the BFKL intercept α^{BFKL} and diffusion constant \mathbf{D}^{BFKL} , see (2.9). Modulo the pomeron intercept and the diffusion constant, which are different (weak coupling or BFKL versus strong coupling or holography), the holographic result in the conformal limit is identical to the BFKL 1-pomeron approximation. Again, the occurrence of the 3/2 exponent reflects on diffusion in $D_\perp = 3$ as noted earlier. It is remarkable that the BFKL resummation of perturbative QCD diagrams is encoded in the stringy Schwinger mechanism discussed in [24], albeit in hyperbolic space.

Figure 3.3 shows the distribution of the holographic wee-dipole density (3.62) in solid line versus \mathbf{b}_\perp for $z = z' = 1.8 \text{ GeV}^{-1}$ and $\chi = 10$. The dashed curve is the asymptotic distribution (3.68). Figure 3.4 shows the distribution

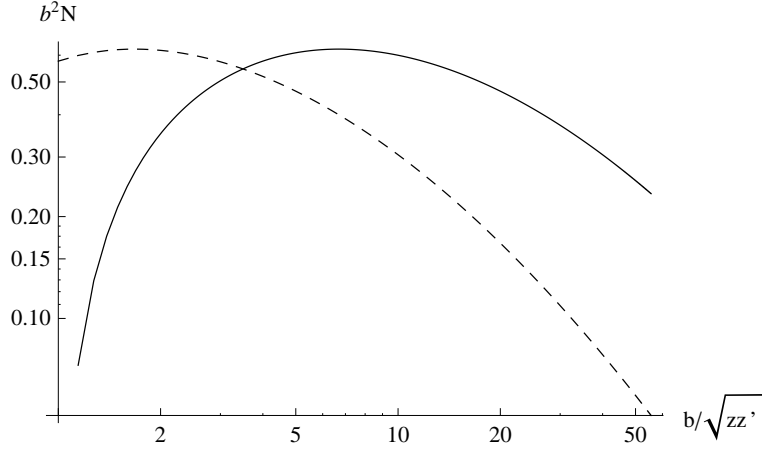


Figure 3.4: BFKL wee-dipole spatial distributions for $z = z' = 1.8 \text{ GeV}^{-1}$ and $\chi = 10$. BFKL density (3.69): solid curve; improved BFKL density: dashed curve. See text.

of the BFKL wee-dipole density (3.69) (solid line) versus $\mathbf{b}_\perp/\sqrt{zz'}$ for also $z = z' = 1.8 \text{ GeV}^{-1}$ and $\chi = 10$. The dashed curve is the improved BFKL result in [38]. The latter follows from (3.69) by inserting a factor of 16 in the argument of the logarithm which corresponds to scaling down the BFKL distribution by a factor of 4 along the $\mathbf{b}_\perp/\sqrt{zz'}$ axis. The holographic results use: $\mathbf{D} = 0.10$ and $\alpha_{\mathbf{P}} - 1 = 0.146$, while the BFKL results use: $\mathbf{D}^{\text{BFKL}} = 0.72$ and $\alpha_{\mathbf{P}} - 1 = 0.477$ with $\lambda = 23$. Both the holographic and the improved distributions are less skewed and more centered. The holographic distribution is less spread than the improved BFKL distribution in \mathbf{b}_\perp , therefore, less infrared sensitive.

3.5 Saturation

In the high energy limit, the total hadronic cross section reaches the unitarity limit. In QCD, this is attributed to the saturation of the scattering objects, leading to a saturation of the scattering amplitudes. We can explain this in the partonic picture, using the example of deep inelastic scattering (DIS), i.e. the process $\gamma^*p \rightarrow X$. There are two parameters describing this process, see Figure 3.5.

1/ The momentum Q of the virtual photon scanning the proton measures the resolution. In pQCD, resolving the partons with higher momentum transfer is done using DGLAP [95, 99, 100].

2/ Bjorken x is the fraction of the momentum carried by the parton struck by the virtual photon. x is related to the center of mass energy by $s = Q^2/x$ and the rapidity relates to x as $Y = \ln(1/x)$. An increase in s increases the rapidity gap. This leads to a decrease in the momentum fraction carried by partons and, thus, an effective increase in the number of partons per unit volume. As the volume of the hadron increases slower ($\sim \ln(s)$, (4.15)) than the number of partons ($\sim s^{\alpha_P-1}$, (3.66)) in it, the partonic wave functions will eventually overlap and the hadron will become “black”. The approach towards the unitarity bound interpreted as an overlapping of partons and hence blackening of the nucleus is called *saturation*. The saturation momentum Q_s , compare dashed line in Figure 3.5, is the typical parton momentum at high energies and yields the average volume of the parton occupied in the hadron. One approach towards the evolution of the scattering amplitude in rapidity is the BFKL approach [7, 8]. Once unitarity corrections become important, this approach has to be modified, leading to the BK equations [101–103].

Saturation in the context of holographic models was also discussed recently in [66, 67] using different arguments. The arguments presented in [66, 67] are based on the Virasoro-Shapiro amplitude in 10 dimensions [25, 26]. As we noted above this construction is far from the pomeron kinematics in confining

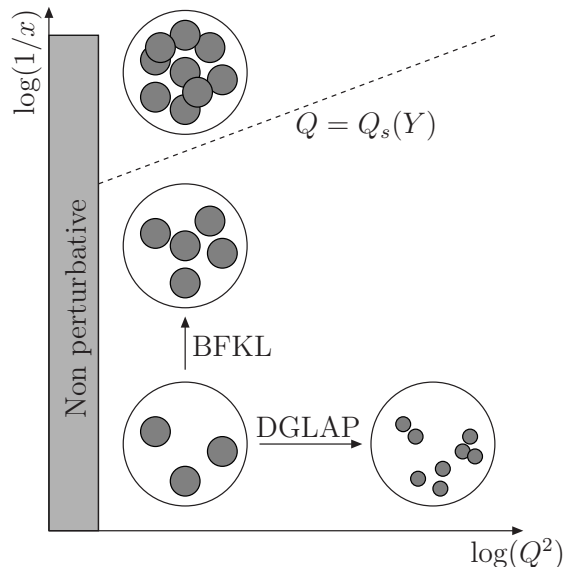


Figure 3.5: Saturation picture of a hadron. From [104].

geometries with massive glueballs. The saturation analysis in [68, 69] makes use of an Euclidean surface that does not contain the stringy Schwinger mechanism with an essential singularity in the limit of a zero rapidity gap. The surface exchanges in [21–24] do. A more model dependent approach to saturation through the use of a black disk approximation for the dipole-dipole cross section in transverse AdS was recently discussed in [71].

In the holographic approach taken here, we make a connection between the following two pictures: The strong coupling (pomeron exchange) dynamics in hadronic scattering on the one hand and the partonic picture of the scattering object where the partons are identified as the wee-dipoles on the other hand.

In curved space the holographic picture suggests the identification of the holographic direction with the effective size of the scatterer [25, 26, 105, 106]. We now suggest that dipole-dipole scattering in holography can be thought of as scattering a wee-dipole cloud of virtuality $1/z$ onto a wee-dipole cloud of virtuality $1/z'$. This leads to the concept of dipole saturation as first discussed in [9].

For $D_\perp = 3$, we identify

$$\frac{aa'}{\alpha'} \mathbf{K}_k(\chi, \mathbf{b}_\perp) \rightarrow zz' \mathbf{N}(\chi, z, z', \mathbf{b}_\perp) . \quad (3.70)$$

In terms of (3.70), the leading ($k = 1$) contribution to (3.9) in a curved AdS background reads

$$\mathbf{W}\mathbf{W} \approx -\frac{g_s^2}{4} (2\pi\alpha')^{3/2} zz' \mathbf{N}(\chi, z, z', \mathbf{b}_\perp) . \quad (3.71)$$

The differential dipole-dipole cross section at finite impact parameter is then [24]

$$\frac{d^4\sigma_{tot}}{dudu'd\mathbf{b}_\perp} = 2 (1 - e^{\mathbf{W}\mathbf{W}}) . \quad (3.72)$$

Assuming that the target is a proton with a dipole wave function peaked at some fixed virtuality corresponding to $u_{\mathbf{T}}$, i.e. $\varphi_{\mathbf{T}}(u') = \delta(u' - u_{\mathbf{T}})$, (3.72) averaged over a target wave function reads

$$\frac{d^3\sigma_{tot}}{du d\mathbf{b}_\perp} \approx 2 (1 - e^{\langle \mathbf{W}\mathbf{W} \rangle}) , \quad (3.73)$$

with only the first cumulant retained and

$$\langle \mathbf{W}\mathbf{W} \rangle = \int dz \varphi_{\mathbf{T}}(z) \mathbf{W}\mathbf{W} . \quad (3.74)$$

Higher cumulants are suppressed by higher powers of $g_s^2 \approx 1/N_c^2$. This amounts to $z' \rightarrow z_{\mathbf{T}}$ in (3.71).

Equation (3.73) suggests the definition of the saturation momentum \mathbf{Q}_s from

$$\frac{d^3\sigma_{tot}}{du_s d\mathbf{b}_\perp} \equiv 2 \left(1 - e^{-z_s \mathbf{Q}_s / (2\sqrt{2})} \right) , \quad (3.75)$$

with $\mathbf{Q}_s \equiv -2\sqrt{2} \langle \mathbf{W}\mathbf{W} \rangle / z_s$ fixed by the saturating dipole size $z_s = \sqrt{2}/\mathbf{Q}_s$. This saturating behavior is illustrated in Figure 3.6. This is the canonical choice for which

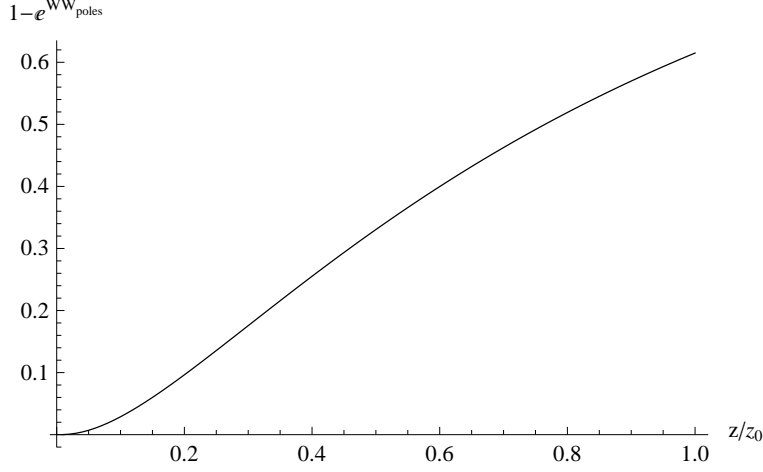


Figure 3.6: Saturating behavior of the dipole-dipole cross section, (3.73), at $\chi = 15$ for fixed $\mathbf{b}_\perp = 2\text{GeV}^{-1}$. ($\mathbf{WW}_{\text{poles}} \equiv \mathbf{WW}$). See text.

$$\left(1 - e^{-z_s \mathbf{Q}_s / (2\sqrt{2})}\right) \rightarrow (1 - e^{-1/2}) \approx 0.4, \quad (3.76)$$

leading to a scattering amplitude of order 1. The saturation momentum follows from the transcendental equation

$$\frac{z_s}{\sqrt{2}} \mathbf{Q}_s(\chi, \mathbf{b}_\perp) = \frac{g_s^2}{2} (2\pi\alpha')^{3/2} z_s z_{\mathbf{T}} \mathbf{N}(\chi, z_s, z_{\mathbf{T}}, \mathbf{b}_\perp) = 1. \quad (3.77)$$

Saturation takes place whenever the dipole density $\mathbf{N} \sim N_c^2/\lambda^{5/4} > 1$ in (hard wall) holography. This is comparable to perturbative QCD with $\mathbf{N} \sim N_c^2/\lambda > 1$. As the dipole density $\mathbf{N}(\chi, z_s, z_{\mathbf{T}}, \mathbf{b}_\perp)$ is peaked around some finite z_s for fixed $\chi, z_{\mathbf{T}}, \mathbf{b}_\perp$, the solution to (3.77) has in general two solutions. To make them explicit, we now need to detail the holographic parameters.

Our set of dimensionless holographic parameters consists of: $D_\perp = 3$, $N_c = 3$, $\lambda = 23$ and $\kappa = 2.5$. The choice of λ is fixed by the F_2 slope in comparison to the DIS data, see section 4.1. The value of κ is fixed by the saturation scale, see below. Since $\lambda = g^2 N_c$, the Yang-Mills coupling is

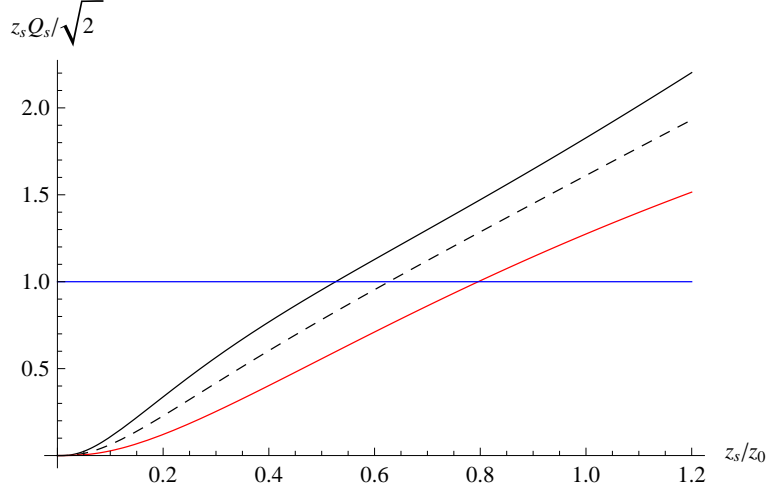


Figure 3.7: Illustration of the solutions to (3.77) with $\mathbf{b}_\perp^2 = 0 \text{ GeV}^{-2}$ (black, solid), $\mathbf{b}_\perp^2 = 1 \text{ GeV}^{-2}$ (black, dashed) and $\mathbf{b}_\perp^2 = 3 \text{ GeV}^{-2}$ (red) at $\chi = 8$. See text.

$g^2/4\pi = 0.6$, which is on the strong coupling side.

We note that although the original string coupling is small, i.e. $\lambda/4\pi N_c = 0.6 < 1$ as required by holography, the physical value of $N_c < \lambda$ is at odds with the holographic and strong coupling limit. This notwithstanding, our corrected soft pomeron intercept is

$$\alpha_{\mathbf{P}} - 1 = \frac{1}{4} - \frac{1}{2\sqrt{\lambda}} = 0.146 . \quad (3.78)$$

Although this numerical value is on the higher side of the pp scattering data of 0.08, it only refers to the bare soft pomeron intercept which is likely to decrease through multipomeron resummation.

Our set of dimensionfull holographic parameters consists of: $z_0 = 2 \text{ GeV}^{-1}$, $z_{\mathbf{T}} = 1.8 \text{ GeV}^{-1}$, $s_0 = 10^{-1} \text{ GeV}^2$, which are set close to the confining scale in QCD. We kinematically translate the rapidity through

$$\chi = \ln \left(\frac{s}{s_0} \right) \equiv \ln \left(\frac{Q^2}{s_0} \left(\frac{1}{x} - 1 \right) \right) \quad (3.79)$$

using the DIS kinematics (see below). For fixed $\chi = 5$ and $z_{\mathbf{T}} = 2$ and varying \mathbf{b}_{\perp} , an illustration of (3.77) is shown in Figure 3.7, using these parameters. The numerical dependence of the slope in Figure 3.7 near the origin (small z_s/z_0) is linear.

3.5.1 Conformal

In the conformal limit, the dipole density is explicit, giving the implicit saturation density

$$\mathbf{Q}_s(\chi, \mathbf{b}_{\perp}) = \frac{g_s^2}{\sqrt{2}} (2\pi\alpha')^{3/2} \frac{1}{z_s} \frac{e^{(\alpha_{\mathbf{P}}-1)\chi}}{(4\pi\mathbf{D}\chi)^{3/2}} \frac{\xi e^{-\frac{\xi^2}{4\mathbf{D}\chi}}}{\sinh(\xi)}. \quad (3.80)$$

For large transverse separation $\frac{\mathbf{b}_{\perp}^2}{2z_s z_{\mathbf{T}}} \gg 1$, (3.80) defines a dipole density in the transverse coordinate

$$\mathbf{Q}_s(\chi, \mathbf{b}_{\perp}) \approx \sqrt{2} g_s^2 (2\pi\alpha')^{3/2} \frac{e^{(\alpha_{\mathbf{P}}-1)\chi}}{(4\pi\mathbf{D}\chi)^{3/2}} \frac{z_{\mathbf{T}}}{\mathbf{b}_{\perp}^2} \ln \left(\frac{\mathbf{b}_{\perp}^2}{z_s z_{\mathbf{T}}} \right) e^{-\ln^2 \left(\frac{\mathbf{b}_{\perp}^2}{z_s z_{\mathbf{T}}} \right) / (4\mathbf{D}\chi)}. \quad (3.81)$$

The large $\chi = \ln(s/s_0) > 1$ exponential asymptotics of (3.80-3.81) have two solutions, say $z_{s1} < z_{s2}$. Only the small dipole solution z_{s1} is retained in the conformal case, as the large dipole solution z_{s2} is deep in the infrared and unphysical. In the confined case, it is naturally cutoff by the wall, see below. With this in mind and to leading exponential accuracy

$$\mathbf{Q}_s(\chi, \mathbf{b}_{\perp}) \approx \frac{z_{\mathbf{T}}}{\mathbf{b}_{\perp}^2} e^{2\mathbf{D}\chi \left(\sqrt{1+(\alpha_{\mathbf{P}}-1)/\mathbf{D}} - 1 \right)}. \quad (3.82)$$

At large $\sqrt{\lambda}$

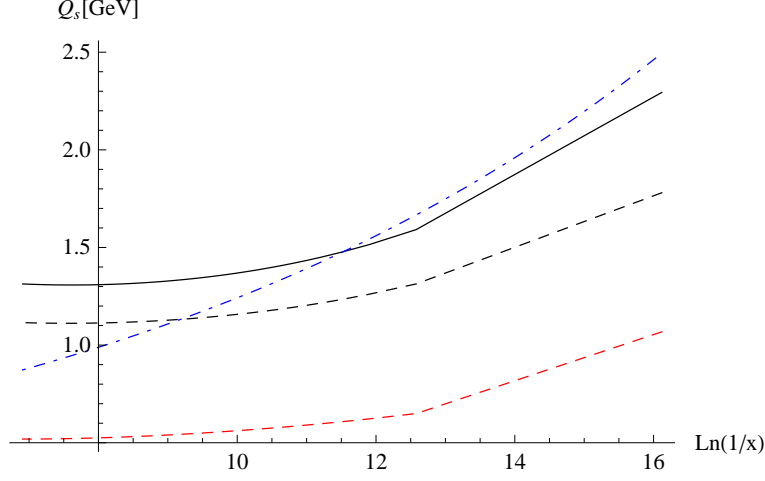


Figure 3.8: x -dependence of the saturation momentum (3.86). Black, solid: $\mathbf{b}_\perp^2 = 0 \text{ GeV}^{-2}$. Black, dashed: $\mathbf{b}_\perp^2 = 1 \text{ GeV}^{-2}$. Dashed red curve: saturation momentum in the conformal limit, (3.80), with $\mathbf{b}_\perp^2 = 1 \text{ GeV}^{-2}$. The dashed dotted blue curve is the GBW saturation momentum from (3.85). See text.

$$\mathbf{Q}_s(\chi, \mathbf{b}_\perp) \approx \frac{z_{\mathbf{T}}}{\mathbf{b}_\perp^2} \left(\frac{1}{x} \right)^{\sqrt{D_\perp/6\sqrt{\lambda}}}, \quad (3.83)$$

illustrating the smallness of the exponent. For the parameters used above, (3.82) reads

$$\mathbf{Q}_s(\chi, \mathbf{b}_\perp) \approx \frac{z_{\mathbf{T}}}{\mathbf{b}_\perp^2} \left(\frac{1}{x} \right)^{0.228/2}. \quad (3.84)$$

An early phenomenological approach to describe DIS data at HERA by Golec-Biernat and Wuesthoff (GBW) in [41], defines the saturation momentum as

$$Q_s^{\text{GBW}}(x) = \left(\frac{x_0}{x} \right)^{\Lambda/2} \text{ GeV}. \quad (3.85)$$

HERA data are fitted with $x_0 = 3.04 \cdot 10^{-4}$ and $\Lambda = 0.288$. Note that the GBW saturation momentum corresponds to the substitution $z_s \mathbf{Q}_s / (2\sqrt{2}) \rightarrow$

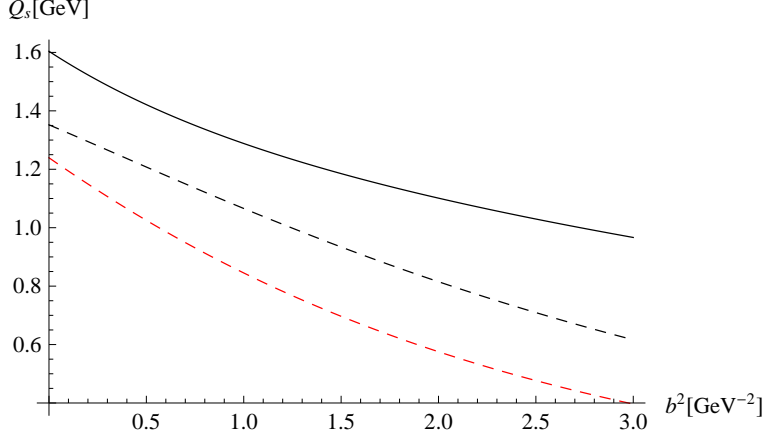


Figure 3.9: Impact parameter dependence of the saturation momentum (3.86). Upper curve (black, solid): $\chi = 5$, lower curve (black, dashed): $\chi = 8$. Lowest curve (red, dashed): Saturation momentum in the conformal limit, (3.80), $\chi = 8$. See text.

$(z_s Q_s^{\text{GBW}}/2)^2$ in (3.75). While the magnitude of the saturation momentum in our holographic approach can be adjusted by tuning κ , we find that the x -dependence of the saturation momentum, (3.84), agrees well with the phenomenological fit in (3.85) as shown in Figure 3.8.

3.5.2 Confining

The identification (3.70) carries over to the confining case. The saturation momentum follows from the transcendental equation

$$\mathbf{Q}_s(\chi, \mathbf{b}_\perp) = \frac{g_s^2}{2} (2\pi\alpha')^{3/2} \frac{e^{(\alpha_{\mathbf{P}}-1)\chi}}{(4\pi\mathbf{D}\chi)^{3/2}} \left(\frac{1}{z_s} \frac{\xi e^{-\frac{\xi^2}{4\mathbf{D}\chi}}}{\sinh(\xi)} + \frac{z_s}{z_0^2} \frac{\xi_* e^{-\frac{\xi_*^2}{4\mathbf{D}\chi}}}{\sinh(\xi_*)} \right). \quad (3.86)$$

The x -dependence of the saturation momentum (3.80), (3.86) is shown in Figure 3.8. Figure 3.9 shows the relevant solution ($z_s \leq z_0$) for the saturation momentum. Note the slow dependence of the holographic saturation momentum on the longitudinal energy in the range $\ln(1/x) \leq 12$. Also note the non-trivial dependence on the impact parameter in the scattering amplitude or \mathbf{Q}_s as opposed to a factorization approach done in most saturation and

color glass-condensate models, compare [\[107\]](#) and references within.

3.6 Stringy Instanton

We will now explain the factor $e^{k\mathbf{b}_\perp^2/2\chi\alpha'}$ in the amplitude (3.34), which drives the Regge behavior [24]. The k th contribution comes from the poles and the pole structure originates from the twist in the longitudinal modes. We will show that the rapidity triggers an electric field acting on the end points of the open string. This is the expected instanton in the pair creation process of the Schwinger mechanism.

We will now employ T-duality along the direction x^1 by setting

$$\partial_\tau x^1 = \partial_\sigma y^1 \tag{3.87}$$

$$\partial_\sigma x^1 = \partial_\tau y^1 . \tag{3.88}$$

In terms of the coordinate y^1 , we can write the boundary conditions (3.14) as a boundary term into the action. In Euclidean and T-dual form [24] the Polyakov string action (3.11) now reads

$$\begin{aligned} S = & \frac{\sigma_T}{2} \int_0^T d\tau \int_0^1 d\sigma ((\partial x^0)^2 + (\partial y^1)^2 + (\partial x^\perp)^2) \\ & + \frac{E}{2} \int_0^T d\tau (y^1 \partial_\tau x^0 - x^0 \partial_\tau y^1) \Big|_{\sigma=0,1} , \end{aligned} \tag{3.89}$$

with

$$E = F_{01} = \sigma_T \tanh(\chi/2) \tag{3.90}$$

a longitudinal electric field along the y^1 direction.

The semiclassical extrema of (3.89) can be labeled by $k > 0$. They follow from the saddle points of (3.89) along T and the world-sheet fields. Explicitly, for $x^\perp = \mathbf{b}_\perp \sigma$

$$x^0 = R(\sigma) \cos(2\pi k\tau/T) \quad , \quad y^1 = R(\sigma) \sin(2\pi k\tau/T) , \tag{3.91}$$

with

$$R(\sigma) = (\mathbf{b}_\perp/\chi) \cosh(\chi(\sigma - 1/2)) . \quad (3.92)$$

The saddle point of (3.89) along the T direction is algebraic, giving $T = 2\pi k/\chi$. A similar world-sheet instanton for D-brane scattering was discussed in [108].

The on-shell action (3.89) now becomes

$$S = \sigma_T 2\pi k \frac{\mathbf{b}_\perp^2}{2\chi} = \frac{k\mathbf{b}_\perp^2}{2\chi\alpha'} \quad (3.93)$$

which reproduces the negative exponent in (3.28).

We note that with Euclidean signature, (3.90) refers to a magnetic field along the transverse 01-direction, so that (3.91) describes a cyclotron motion of the string instanton in the 01-plane with cyclotron frequency $\omega_k = 2\pi k/T$. With Minkowski signature, the motion is hyperbolic with local acceleration

$$a(\sigma) = \frac{1}{R(\sigma)} = \frac{\chi}{\mathbf{b}_\perp} \frac{1}{\cosh(\chi(\sigma - 1/2))} , \quad (3.94)$$

which has a maximum at the center of the open string, $\sigma = 1/2$.

3.7 Schwinger mechanism and Unruh phenomenon

Schwinger showed in '51 [109] that a strong electric field can pair produce charged particles. Consider scalar QED, coupling charged massive particles with charge e and mass m to a strong electric field E . The Euclidean action acquires an imaginary part

$$Im S_{QED} = \frac{\pi m^2}{eE} , \quad (3.95)$$

which yields the tunneling probability

$$\Gamma_{vacuum \rightarrow m} \sim e^{-ImS} = e^{-\frac{\pi m^2}{eE}} . \quad (3.96)$$

The acceleration of the on-shell particle under the influence of the electric field is

$$a = eE/m \quad (3.97)$$

and (3.96) can be interpreted as

$$\Gamma_{vacuum \rightarrow m} \sim e^{-\frac{\pi m}{a}} . \quad (3.98)$$

Charged particles are experiencing a constant acceleration and the classical Euclidean orbits are closed trajectories. From (3.95) and (3.96) we readily obtain the (proper) Euclidean time needed to complete the orbit

$$\tau_{Euclidean} = \partial_m ImS_{QED} = \frac{2\pi}{a} . \quad (3.99)$$

Unruh [110] observed that a constantly accelerated observer experiences a ground state that has the characteristics of a thermal ensemble, characterized by an Unruh temperature T_U given by

$$T_U = \frac{a}{2\pi} . \quad (3.100)$$

We have seen in chapter 3.6 that the open string experiences an acceleration

which is maximal midway between the two surfaces. This allows us to assign an Unruh temperature to the scattering process. To make this more explicit, we will use our gravitational setup and show that the induced geometry on the string world-sheet is indeed a Rindler frame. The Rindler frame can be interpreted as the near horizon geometry of a (Schwarzschild) black hole, which then introduces an (Unruh) temperature.

Indeed, the line element associated to the instanton (3.91) in Minkowski signature is

$$ds^2 \approx -a^2 R^2 d(\tau \mathbf{b}_\perp)^2 + dR^2 + dx^\perp{}^2 \quad (3.101)$$

with Rindler time $t(\tau) = \tau \mathbf{b}_\perp$. The Rindler acceleration $a = \chi/\mathbf{b}_\perp$ implies a Rindler horizon $\mathbf{R} = 1/2a$. Due to this acceleration, the string feels a σ -dependent Unruh temperature $T_U(\sigma) = a(\sigma)/2\pi$ that is maximal at the center with $T_U = \chi/2\pi \mathbf{b}_\perp \equiv 1/\beta$. Initially, this temperature is only felt in the longitudinal direction. For small rapidities, $\chi \sim 1$, the scattering process is dominated by $\mathbf{b}_\perp \sim l_s \sim 1/m$, and (3.94), (3.90) equate to the classical result of a point particle (3.97)

$$a \sim \frac{1}{\mathbf{b}_\perp} \frac{\chi}{\cosh(\chi)} \sim \frac{\sigma}{m} \tanh(\chi) \sim E/m . \quad (3.102)$$

In this regime, the saturation momentum for short strings ($\xi \ll 1$) asymptotes $\mathbf{Q}_s \sim \chi/l_s \sim a$ and we recover the familiar result using a classical QCD approach [111].

3.8 Entropy

We have seen in section 3.6 that the stringy instanton solution (3.91) reduces the on-shell action to (3.93)

$$S_k \approx \frac{1}{2} \sigma_k \mathbf{b}_\perp \beta, \quad (3.103)$$

with the k-string tension $\sigma_k = k\sigma_T$ for N-ality k and $\beta = 1/T_U = 2\pi\mathbf{b}_\perp/\chi$. For QCD with 3 colors, only the N-alties $k = 1, 2$ are allowed. For QCD at large N_c , all N-alties up to the integer value of $N_c/2$ are allowed. Only the N-ality $k = 1$ is selected in the process of scattering dipoles in the fundamental representation. In section 4.4 we argue that $k = 2$ is released in *dense AA* collisions.

Equation (3.103) receives quantum contributions that are captured by Gribov diffusion at strong coupling. For large χ and \mathbf{b}_\perp , the quantum ($\mathcal{O}(n)$) and curvature ($\mathcal{O}(1/\sqrt{\lambda})$) corrections are readily implemented by the diffusive nature of the propagator.

The dominant quantum correction follows from the transverse diffusion of the tachyonic mode ($n = 0$) in AdS_{D_\perp} . To order $1/\sqrt{\lambda}$ the onshell string action (3.11) reads [24]

$$S_k \approx \frac{k}{4\pi} \xi^2 \frac{\beta}{\mathbf{b}_\perp} - 2\pi \frac{\mathbf{b}_\perp}{\beta} \left(\frac{D_\perp}{12k} - \frac{(D_\perp - 1)^2}{8\sqrt{\lambda}} \right). \quad (3.104)$$

This Euclidean stringy action amounts to a free energy $F_k = S_k/\beta$. It follows that (3.104) carries an entropy

$$\mathbf{S}_k \equiv \beta^2 \frac{\partial F_k}{\partial \beta} \approx \chi \left(\frac{D_\perp}{6k} - \frac{(D_\perp - 1)^2}{4\sqrt{\lambda}} \right) \quad (3.105)$$

or equivalently

$$\mathbf{S}_k \approx 2(\alpha_{\mathbf{P}k} - 1)\chi. \quad (3.106)$$

For $k = 1$, the pomeron intercept is $(\alpha_{\mathbf{P}1} - 1) \approx 0.15$ and the entropy per unit rapidity is about $1/3$. Using the optical theorem, the virtual wee-dipoles become on-shell and their contribution to the entropy gives

$$\mathbf{S}_k \approx \ln N_{wee,k}^2, \quad (3.107)$$

where $N_{wee,k}$ is the total number of wee-dipoles surrounding each of the incoming dipole pairs involved in the collision, compare section 3.4.3

$$N_{wee,k} = \int dud\mathbf{b}_\perp \mathbf{N}_k = e^{(\alpha_{\mathbf{P}k}-1)\chi}. \quad (3.108)$$

This is to be contrasted with the fully thermal or incoherent expectation of $\ln N$ and the fully Poissonian or coherent expectation of $\ln\sqrt{N}$, with N the mean multiplicity number.

Most of this entropy is the result of the tachyon excitation on the string. Indeed, for large impact parameter \mathbf{b}_\perp , the Unruh temperature is smaller than the Hagedorn temperature,

$$T_U = \frac{\chi}{2\pi\mathbf{b}_\perp} < T_H = \sqrt{\frac{3\sigma_T}{\pi D_\perp}}, \quad (3.109)$$

which translates to $\mathbf{b}_\perp > \chi/(2\pi T_H)$. As the impact parameter is reduced, the Unruh temperature increases, causing the string excitations to exponentiate, leading to a Hagedorn transition. At the Hagedorn point it may be mapped on the Bekenstein-Hawkins (BH) temperature of a microscopic black hole [112–115].

3.9 Formation time

Over what time is the entropy (3.106-3.107) associated with the dipole-dipole collision released? To answer this question, we note that the emergence of an Unruh temperature on the string world-sheet suggests that semiclassically the metric is locally Rindler, see (3.101).

We suggest that the prompt release time t_R can be set to be the time when the diffusing string in transverse AdS_{D_\perp} reaches the effective size of the Rindler horizon \mathbf{R} by analogy with the time it takes for a string to fall on a black hole [113, 116]. Indeed, the string diffusion in rapidity causes the transverse string size to increase as

$$\langle x_\perp^2 \rangle = \chi \alpha' \equiv \mathbf{D}_R t(1) , \quad (3.110)$$

with the diffusion constant in Rindler space $\mathbf{D}_R = \alpha'/(2\mathbf{R})$. Through the last equality, we reinterpret (3.110) as a diffusion in Rindler space over a typical Rindler time $t(1) = \mathbf{b}_\perp$. The release entropy time t_R is then set by the condition $\langle x_\perp^2 \rangle|_{t=t_R} = \mathbf{R}^2 = \mathbf{D}_R t_R$ or $t_R = 2\mathbf{R}^3/\alpha'$. For a QCD string with $\alpha' = 1/(2 \text{ GeV})^2 = (0.1 \text{ fm})^2$ and a typical impact parameter $\mathbf{b}_\perp \sim 10\sqrt{\alpha'}$, this results in $t_R \sim (25 \text{ fm})/\chi^3$, which is short.

Chapter 4

Comparison to experiment

The parameters of our holographic dipole scattering approach are

- dimension D_{\perp} of the transverse space
- t'Hooft coupling λ
- string coupling g_s
- IR cut-off z_0
- typical onium mass $\sqrt{s_0}$

A comparison to experimental data will allow us to fix the parameters of our model and test it against further data. In addition, we will see that the obtained values for the parameters are within reasonable agreement when compared to QCD expectations.

A comparison to DIS data on the proton structure function F_2 allows us to fix both the transverse dimensionality of the space and the t'Hooft coupling. In our approach, the scaling of the structure function with the momentum transfer crucially depends on the dimensionality of the transverse space, and a comparison to the measured Q^2 dependence of F_2 fixes D_{\perp} . From the scaling of the structure function with x , we can fix the t'Hooft coupling. Diffractive pp scattering allows us to get a better fit on the IR cut-off and the string coupling. The data is relatively insensitive to the precise value of the onium mass.

4.1 Deep inelastic scattering

Deep inelastic scattering (DIS) of a lepton on a proton target can be viewed as a small size dipole scattering through a proton [30–36]. A holographic approach to DIS starting from the graviton limit and based on the critical string amplitude was elaborated in [105, 106], see also [117].

The dipole-dipole cross section is useful for the determination of the inclusive proton structure function $F_2(x, Q^2)$ for small Bjorken x and large Q^2 . Specifically [35, 36],

$$F_2(x, Q^2) = \frac{Q^2}{4\pi^2\alpha_{EM}} (\sigma_T + \sigma_L) , \quad (4.1)$$

with the electromagnetic fine structure constant α_{EM} . $\sigma_T + \sigma_L = \sigma_{\text{tot}}$ can be regarded as the total (virtual) photon-to-proton or dipole-to-dipole cross section. By the optical theorem

$$\sigma_{\text{tot}}(s) = -\frac{1}{s} \text{Im} \mathcal{T}(s, t = 0) , \quad (4.2)$$

whereby

$$\mathcal{T}(s, 0) = -2is \int d\mathbf{b}_\perp du du' \varphi_{\mathbf{P}}(u) \varphi_{\mathbf{T}}(u') (1 - e^{\mathbf{w}\mathbf{w}}) , \quad (4.3)$$

which is an averaging of the zz' -dipole-dipole cross-section over the target $\varphi_{\mathbf{T}}(u')$ and projectile $\varphi_{\mathbf{P}}(u)$ dipole wave functions respectively. Thus,

$$F_2(x, Q^2) = \frac{Q^2}{2\pi^2\alpha_{EM}} \int d\mathbf{b}_\perp du du' \varphi_{\mathbf{P}}(u) \varphi_{\mathbf{T}}(u') (1 - e^{\mathbf{w}\mathbf{w}}) . \quad (4.4)$$

The integration in (4.3), (4.4) involve all values of the impact parameter. While the validity of our approach following [24] is for large \mathbf{b}_\perp , we note that the dominant contribution to (4.3), (4.4) stems from $\mathbf{b}_\perp \sim \sqrt{\alpha'\chi}$, which is large. Typically, the (target) proton and (projectile) photon dipole distributions are

peaked, say

$$\varphi_{\mathbf{P}}(u) \equiv (\alpha_{EM}/\kappa^2) \delta(u - u_{\mathbf{P}}) \quad (4.5)$$

$$\varphi_{\mathbf{T}}(u') \equiv \delta(u - u_{\mathbf{T}}) . \quad (4.6)$$

The normalization of the projectile (current) distribution in (4.5) is fixed empirically by the magnitude of the measured structure function F_2 . Of course, (4.6) are schematic wave functions that nonetheless capture the key physics and allow for analytical integration. We expect only small modifications if more realistic wave functions are used.

Inserting (4.6) into (4.4) and using the dipole-dipole cross-section for $D_{\perp} = 3$ yields in the 1-pomeron exchange limit for the conformal case

$$F_2(x, Q^2) \Big|_{\text{conformal}} \approx \frac{g_s^2}{8\pi^2\kappa^2} (2\pi\alpha')^{3/2} z_{\mathbf{T}} Q \frac{e^{(\alpha_{\mathbf{P}}-1)\chi}}{\sqrt{4\pi\mathbf{D}\chi}} \left(e^{-\frac{1}{4\mathbf{D}\chi}\ln^2(Qz_{\mathbf{T}})} \right) \quad (4.7)$$

and in the confining case

$$F_2(x, Q^2) \Big|_{\text{confining}} \approx \frac{g_s^2}{8\pi^2\kappa^2} (2\pi\alpha')^{3/2} z_{\mathbf{T}} Q \frac{e^{(\alpha_{\mathbf{P}}-1)\chi}}{\sqrt{4\pi\mathbf{D}\chi}} \left(e^{-\frac{1}{4\mathbf{D}\chi}\ln^2(Qz_{\mathbf{T}})} + e^{-\frac{1}{4\mathbf{D}\chi}\ln^2(Qz_0^2/z_{\mathbf{T}})} \right) , \quad (4.8)$$

with $u_{\mathbf{P}} = \ln(z_0Q)$, $u_{\mathbf{T}} = \ln(z_0/z_{\mathbf{T}})$. We have used the fact that

$$\mathbf{N}(T_{\perp}, u, u', t = 0) = \frac{e^{-T_{\perp}(M_0^2+1)}}{\sqrt{4\pi T_{\perp}}} \left(e^{-(u'-u)^2/4T_{\perp}} + e^{-(u'+u)^2/4T_{\perp}} \right) \quad (4.9)$$

for $t = -\mathbf{q}_{\perp}^2 = 0$, after making use of the Fourier transform

$$\mathbf{N}(T_{\perp}, u, u', \mathbf{q}_{\perp}^2) = \int d\mathbf{b}_{\perp} e^{i\mathbf{q}_{\perp} \cdot \mathbf{b}_{\perp}} \mathbf{N}(T_{\perp}, u, u', \mathbf{b}_{\perp}) . \quad (4.10)$$

Since the diffusion kernel in (4.9) is generic, the Q^2 dependency of the structure function is sensitive to the \perp -dimensions considered, $\mathbf{N} = \Delta/(zz')^{D_{\perp}-2}$.

The above approximation is justified when the photon momentum is sufficiently larger than the saturation scale, $Q \geq \mathbf{Q}_s$, at all impact parameters

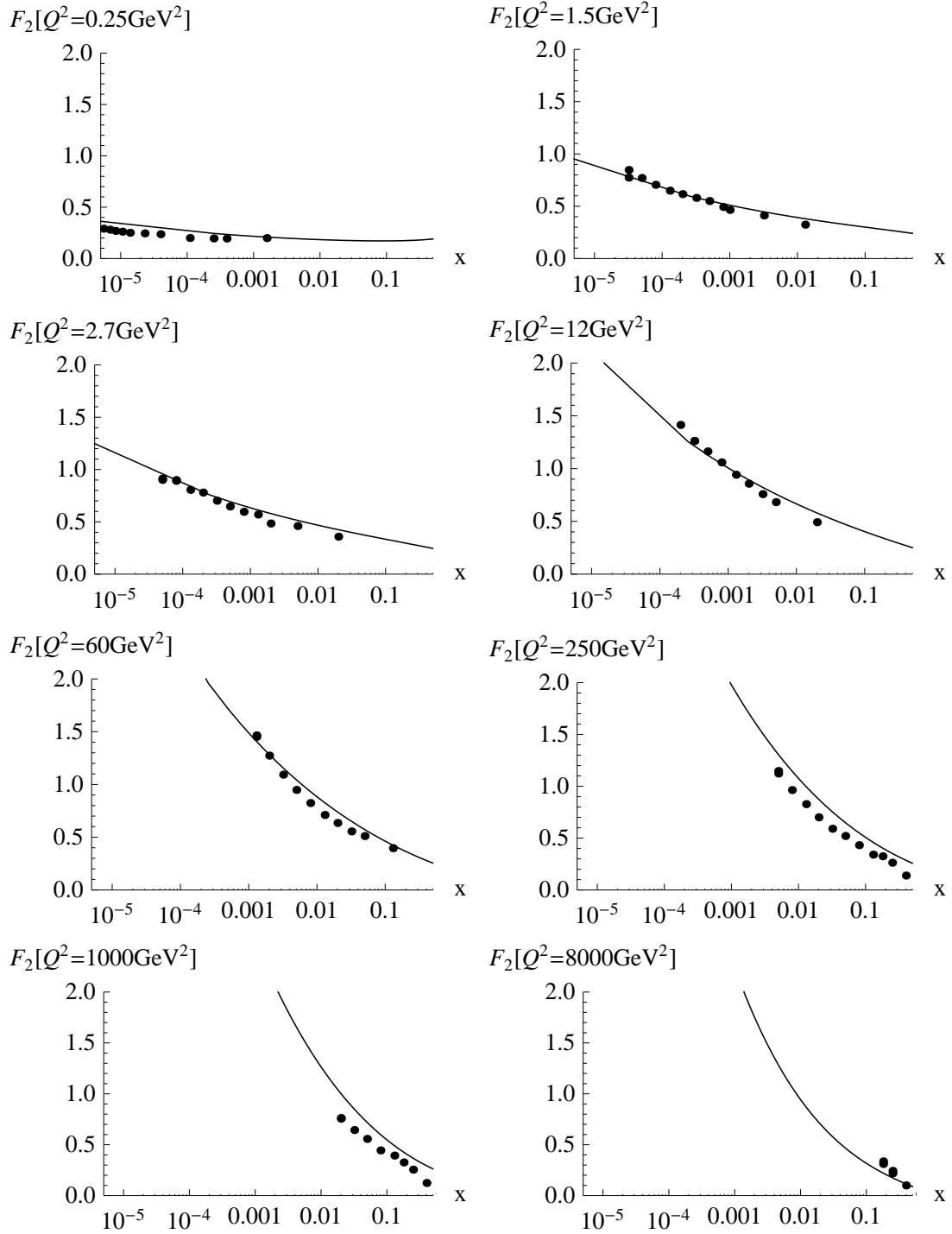


Figure 4.1: Proton structure function F_2 in the confining background, (4.8). See text.

\mathbf{b}_\perp . For the range of values for Q^2 and x considered to compare to the HERA data, the value for the proton structure function F_2 using the exponentiated 1-pomeron exchange, (4.4), differs by less than 8% compared to F_2 from (4.8).

Figure 4.1 compares our result (4.8) to the HERA data [118], using the following holographic parameter set:

- $D_\perp = 3$
- $N_c = 3$
- $\lambda = 23$
- $\kappa = 2.5$
- $z_{\mathbf{T}} = 1.8 \text{ GeV}^{-1}$
- $z_0 = 2 \text{ GeV}^{-1}$
- $s_0 = 10^{-1} \text{ GeV}^2$

With our choice of parameters, our result for the 1-pomeron exchange amplitude in the confining background appears to fit the DIS data overall. Note that for $z_0 \sim z_{\mathbf{T}}$, the contribution from the hard wall is comparable to the conformal contribution. Thus, the conformal result (4.7) alone is not sufficient to describe the data with our set of parameters. Clearly our analysis is only qualitative, and a more thorough study of the parameter dependences and the fitting accuracy are needed.

Finally, we note that the transcendental equation for the saturation momentum, (3.77), defines the saturation line as a separatrix between the dilute and dense wee-dipole environments. For fixed virtuality Q^2 (inverse dipole size squared) and impact parameter \mathbf{b}_\perp , Figure 4.2 shows the rapidities at which the cross section saturates in the black solid and dashed curves, i.e. when the condition in (3.77) is fulfilled. For comparison, the Golec-Biernat Wuesthoff result in (3.85) is shown as the blue solid curve. The points are the measured HERA data for the F_2 structure function. We note that (3.77) admits in general 2 distinct solutions for fixed x, Q^2 or χ , but only the one with the largest χ is shown which is warranted by our approximations. The HERA points at the

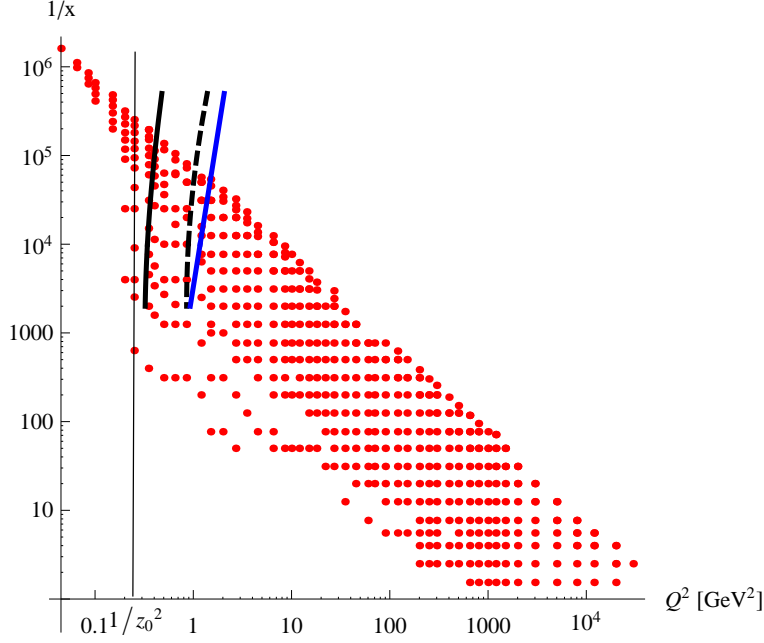


Figure 4.2: Saturation lines in the confining background for $\mathbf{b}_\perp = 0 \text{ GeV}^{-1}$ (black, dashed curve) and $\mathbf{b}_\perp = 2 \text{ GeV}^{-1}$ (black, solid curve) in comparison to the Golec-Biernat Wuesthoff result, (3.85), (blue, solid). The confining wall is at $1/z_0^2 = 1/4$. The dots are the measured HERA data. See text.

left of the confining wall $1/z_0^2 = 1/4$ are well within the confining region. The confined holographic saturation lines are *stiff* in longitudinal energy as already noted in Figure 3.8 above. For $\mathbf{b}_\perp = 0$ the HERA points to the far right of the saturation line are well within the perturbative or dilute wee-dipole phase. Those close or to the left of the saturation line correspond to the saturated wee-dipole phase. The closer they are to the confining wall $1/z_0^2 = 1/4$ the less perturbative they are in nature. The holographic saturation lines show that a large swath of the measured points at HERA which are well within the holographic saturation domain are sensitive to the impact parameter dependence \mathbf{b}_\perp of the saturation scale.

4.2 Diffractive pp scattering

Diffractive proton-proton scattering at small momentum transfer unravels information about the transverse shape of the proton and the large $|t|$ behavior probes length scales of the typical string length, which in the confining background is of the order of z_0 . We will fit the effective dipole size of the proton, z_p , and the position of the hard wall, z_0 , to the data. All other numerical values remain the same as in section 4.1.

In the eikonal approximation the differential cross section reads

$$\frac{d\sigma_{ap \rightarrow bp}}{dt}(\chi, |t|) = \frac{1}{16\pi s^2} |\mathcal{T}(\chi, |t|)|^2 \quad (4.11)$$

$$= \frac{1}{4\pi} \left| i \int d\mathbf{b}_\perp \int du \int du' e^{iq_\perp \cdot \mathbf{b}_\perp} |\psi_{ab}(u)|^2 |\psi_p(u')|^2 (1 - e^{\mathbf{w}\mathbf{w}}) \right|^2 \quad (4.12)$$

$$= \frac{\pi}{4} \left| i \int d|\mathbf{b}_\perp|^2 \int du \int du' J_0(\sqrt{|\mathbf{b}_\perp|^2 |t|}) |\psi_{ab}(u)|^2 |\psi_p(u')|^2 (1 - e^{\mathbf{w}\mathbf{w}}) \right|^2 \quad (4.13)$$

with $t = -q_\perp^2$. Here, J_0 is the Bessel function and the overlap amplitude is defined by $|\psi_{ab}(u)|^2 \equiv \psi_a^*(u)\psi_b(u)$.

Instead of using diffractive eigenstates [119], [120], perturbative [75], [121] or holographic light-front wave functions [43, 44], we will fit the data assuming the proton distribution is identified with the wee-dipole distribution, i.e. the proton is sharply peaked at some scale $1/z_p = \frac{e^{-u_p}}{z_0}$, [105]. More explicitly, the square of the wave function will be approximated by a delta-function, $|\psi_p(u)|^2 = \mathcal{N}_p \delta(u - u_p)$. We treat the normalization constant \mathcal{N}_p that carries the dipole distribution to the physical proton distribution as a parameter to be fitted to the data.

4.2.1 Comparison to data: ISR

A comparison of the differential elastic pp cross section, (4.13), to the CERN ISR data [122] is made by fitting the position of the dip and the slope

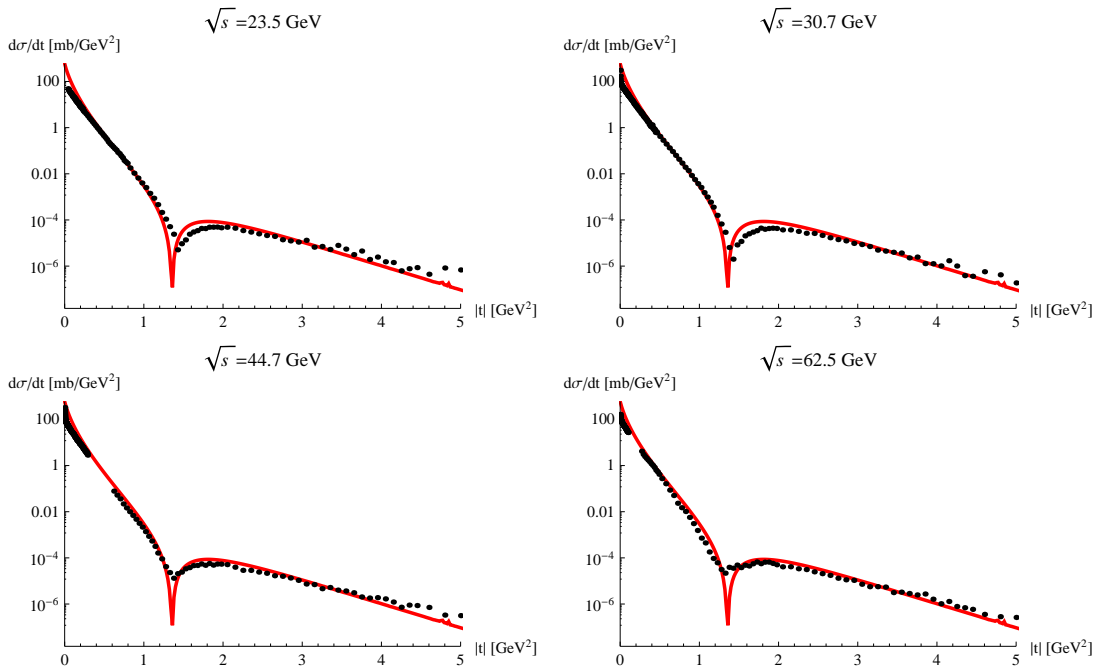


Figure 4.3: Differential pp cross section. Dots: data from CERN ISR. Solid line: holographic result. See text.

of the shoulder region ($|t| > 1.5 \text{ GeV}^2$). We use the full, unitary amplitude including higher order terms in the eikonal \mathbf{WW} . The importance of higher order terms in the eikonalized amplitude was also noted in [123]. A fit yields $z_0 = 2 \text{ GeV}^{-1}$ and $z_p = 3.3 \text{ GeV}^{-1}$, see Figure 4.3. To leading order, the position of the (first) dip is sensitive to the effective size of the scatterer and the energy of the scattering object. It scales with $1/(\mathbf{D}\chi z_p^2)$ and occurs at relatively low $|t|$ with primary sensitivity to the size of the proton, z_p .

At high momentum transfer ($|t| > 2 \text{ GeV}^2$), the typical length scales probed are of the size of the fundamental string length, which is of the order of the IR cut-off. Thus, the slope of the shoulder region is fitted by primarily adjusting the value of the confinement scale z_0 . The result for the cross section in the conformal limit $z_0 \rightarrow \infty$ does not yield a reasonable fit to the data. Note that unlike perturbative QCD reasoning [124] where the partons are resolved at large $|t|$ leading to a power-like decrease, the slope of the cross section at $|t| \geq 2 \text{ GeV}^2$ is essentially not power-like in our holographic model.

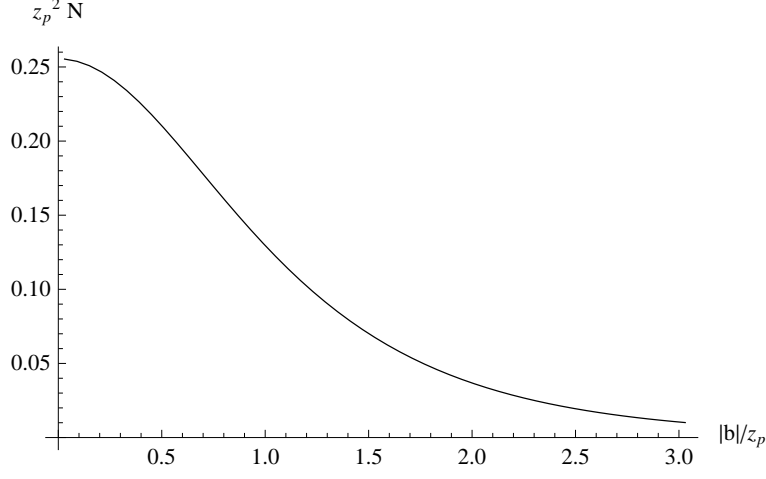


Figure 4.4: Transverse distribution of the wee-dipole density \mathbf{N} , (3.62), with $\sqrt{s} = 20 \text{ GeV}$.

The result $z_p > z_0$ violates the construction of the cut-off through a hard wall at z_0 . While the implementation of confinement in AdS/QCD through a hard-wall has well-known difficulties describing some features of QCD, this toy model is nonetheless useful as it simplifies most computations and captures the essential features of the theory described. The cut-off through the hard-wall has to be relaxed in order to fit the data in the high $|t|$ region.

At $|t| \sim 0 \text{ GeV}^2$, the slope parameter $B(s, |t|)$ gives the mean square proton radius

$$\begin{aligned}
 B(s, |t| = 0) &\equiv \left(\frac{d}{dt} \ln \left(\frac{d\sigma_{pp \rightarrow pp}}{dt}(s, t) \right) \right) \Big|_{t=0} = \frac{1}{2} \frac{\int d|\mathbf{b}_\perp|^2 |\mathbf{b}_\perp|^2 (1 - e^{\mathbf{w}\mathbf{w}})}{\int d|\mathbf{b}_\perp|^2 (1 - e^{\mathbf{w}\mathbf{w}})} \\
 &= \frac{1}{2} \langle |\mathbf{b}_\perp|^2 \rangle
 \end{aligned} \tag{4.14}$$

The wee-dipole density \mathbf{N} is peaked at $\frac{\mathbf{b}_\perp}{z_p}$ small, see Figure 4.4, and expanding the exponential in 4.13 to first order in g_s^2 gives

$$B(s) \sim \mathbf{D}\chi (z_p^2 + z_0^2) . \tag{4.15}$$

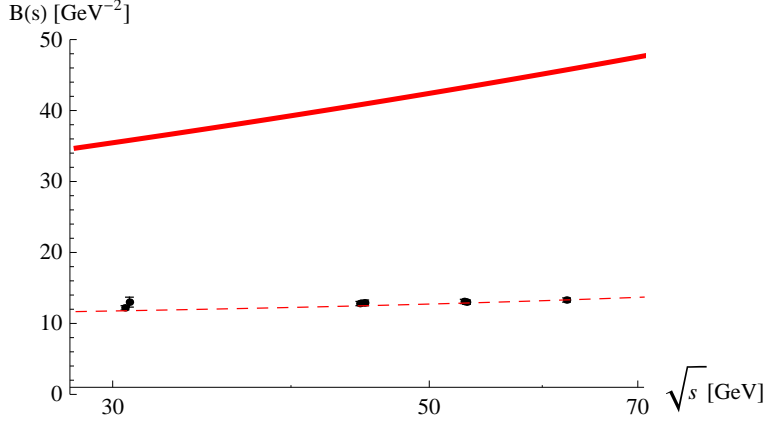


Figure 4.5: Experimental data for the slope parameter in comparison with the holographic result for the slope parameter, (4.14), for $|t| = 0 \text{ GeV}^2$ (red, solid) and $|t| = 1 \text{ GeV}^2$ (red, dashed). See text.

The radius of the proton is not only proportional to the effective wee-dipole size z_p but also receives contributions from the IR cut-off. At strong coupling, the diffusive nature of the eikonized scattering amplitude is responsible for the scaling of the proton radius with the rapidity, $B(s) \sim \mathbf{D}\chi \sim \frac{1}{\sqrt{\lambda}} \ln\left(\frac{s}{s_0}\right)$.

In the approach taken here, the transverse structure of the proton is modelled by a cloud of wee-dipoles surrounding a parent dipole. We can easily understand the scaling of the proton size with the coupling. As the coupling increases, the diffusion constant decreases, which results in the outer part of the cloud becoming more dilute and, hence, the proton shinks.

Figure 4.5 shows the slope parameter for $|t| = 0 \text{ GeV}^2$ and $|t| = 1 \text{ GeV}^2$. In our setup, the momentum distribution between the two constituents of each dipole is symmetric resulting in a small-size dipole, whereas asymmetric, large-size pairs dominate the small $|t|$ region, see e.g. [78]. Thus, we suspect large-size dipoles to dominate the region $|t| \leq 1 \text{ GeV}^2$. The Coulomb contribution to the scattering amplitude can be neglected in the kinematic region $|t| > 0.01 \text{ GeV}^2$ [125, 126].

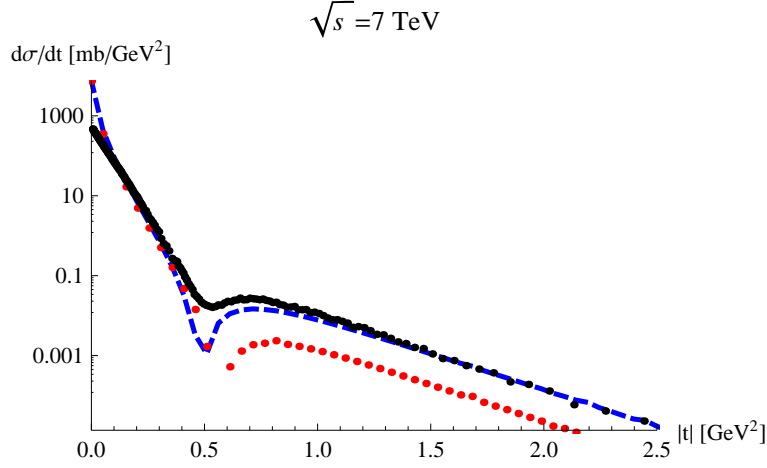


Figure 4.6: Differential pp cross section. Black dots: data from the TOTEM experiment at LHC. Dashed blue line and red dots: holographic result. See text.

4.2.2 Comparison to data: LHC

Elastic pp scattering at LHC energies of $\sqrt{s} = 7 \text{ TeV}$, allows us to test the energy dependence of our model. With the numerical values fitted at energies $\sqrt{s} \sim 20 - 60 \text{ GeV}$, the fit (red line) in Figure 4.6 indicates a mismatch in the energy dependence of the holographic model. In order to get a better fit to the LHC data, the parameters governing the coupling (λ), the effective size of the proton (z_p) have to be slightly altered. The fit (blue, dashed line) in Figure 4.6 is obtained with: $\lambda = 24.5$, $z_p = 3.5 \text{ GeV}^{-1}$, $\mathcal{N}_p = 0.0257$.

4.3 Deeply virtual Compton scattering (DVCS)

At high energies, DVCS is dominated by pomeron exchange. In the rest frame of the proton, the virtual photon fluctuates into a quark-antiquark dipole that interacts with the proton. We will now use the holographic dipole-dipole amplitude to access the differential DVCS cross section $\frac{d\sigma_{\gamma^*p \rightarrow \gamma p}}{dt}$, (4.13). In the above section we have refined the numerical values governing the transverse shape of the proton (z_p) and the IR cut-off scale (z_0) for the energy range of $\sqrt{s} \sim 20 - 60 \text{ GeV}$. We will use these values to analyze the DVCS data in the range $\sqrt{s} \sim 40 - 100 \text{ GeV}$. Now that all parameters of the holographic cross section are fixed, a comparison to the DVCS data serves as an additional test for our model.

The $\gamma^*\gamma$ overlap amplitude, $|\psi_{\gamma^*\gamma}(u)|^2$, is approximated by a delta function, peaked at some finite virtuality $Q = 1/z$. With the effective size of the proton, $z_p = 3.3 \text{ GeV}^{-1}$, the position of the cut-off, $z_0 = 2 \text{ GeV}^{-1}$, and the normalization $\mathcal{N}_p = 0.0257$ fixed, we compare our holographic result to the HERA data. Figure 4.7 illustrates an agreement of the cross section obtained from the holographic dipole-dipole scattering amplitude with the data.

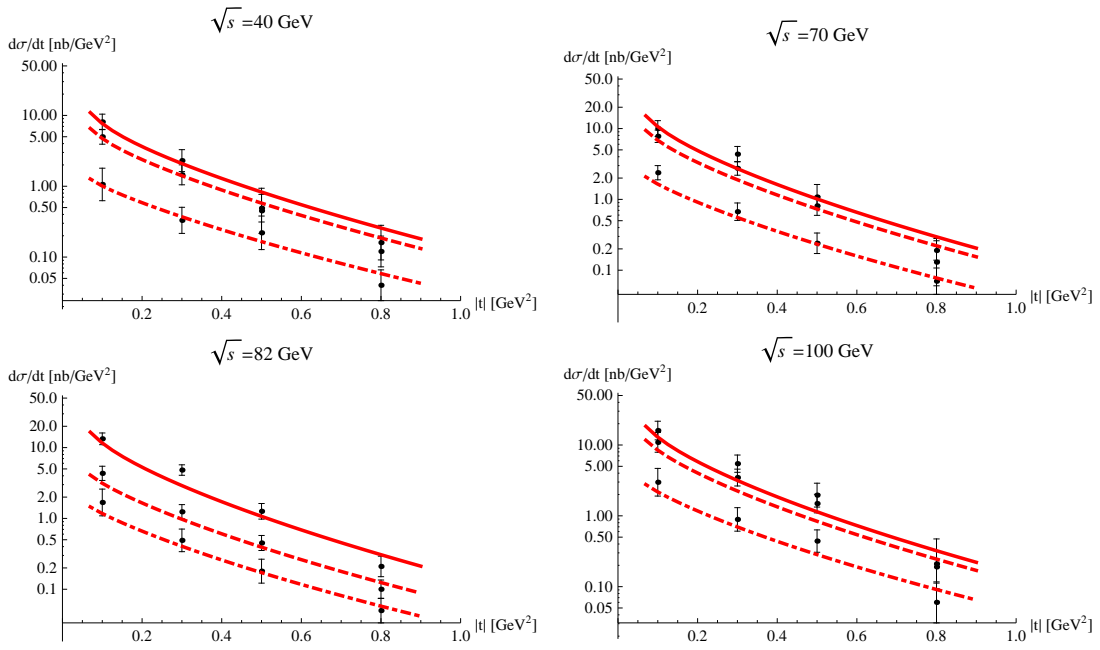


Figure 4.7: Holographic result for the differential DVCS cross section compared to the HERA data [127–129]. $\sqrt{s} = 82$ GeV: solid - $Q^2 = 8$ GeV², dashed - $Q^2 = 15.5$ GeV², dotted - $Q^2 = 25$ GeV². $\sqrt{s} = 40, 70, 100$ GeV: solid - $Q^2 = 8$ GeV², dashed - $Q^2 = 10$ GeV², dotted - $Q^2 = 20$ GeV². See text.

4.4 Multiplicities

In dipole-dipole scattering at large rapidity, the induced instanton on the string world-sheet carries entropy $\mathbf{S}_k = 2(\alpha_{\mathbf{P}k} - 1)\chi$, see section 3.8, with $\alpha_{\mathbf{P}k} - 1$ the pomeron intercept for a dipole source of N-ality k . This stringy entropy is neither coherent nor thermal. We argued in section 3.9 that it is released promptly over a time $t_R \approx (\mathbf{b}_\perp/\chi)^3/(4\alpha')$ with $\alpha'/2$ the pomeron slope and \mathbf{b}_\perp the impact parameter. Below we will show that this stringy entropy may explain the 3/2 jump in the total charged multiplicities at about 10 participants reported over a wide range of collider energies by PHOBOS. We predict the charged multiplicities in pp , pA and central AA collisions at LHC.

The issue of how entropy is released in hadron-hadron and nucleus-nucleus collisions is a fundamental problem in the current heavy-ion program at collider energies. How coherence, which is a hallmark of a fundamental collision, turns to incoherence, which is at the origin of the concept of entropy, is a theoretical question of central importance. A possible understanding for the entropy deposition was attempted at weak coupling through the concept of the color glass approach in classical but perturbative QCD [53–55] and at strong coupling through the concept of black hole formation in holographic QCD [56–60].

The evidence of a strongly coupled plasma released at collider energies, with large and prompt entropy deposition and flow, suggest that a strong coupling approach is needed for the mechanism of entropy decomposition. In this way, the holographic approach with the release of a black hole falling along the holographic direction provides a plausible mechanism for entropy production. However, this mechanism is detached from our understanding of fundamental pp collisions, which are, after all, the seeds at the origin of the entropy production.

pp collisions can be viewed as dipole-dipole scattering from each colliding proton. The density of dipoles in the proton is set by the saturation momen-

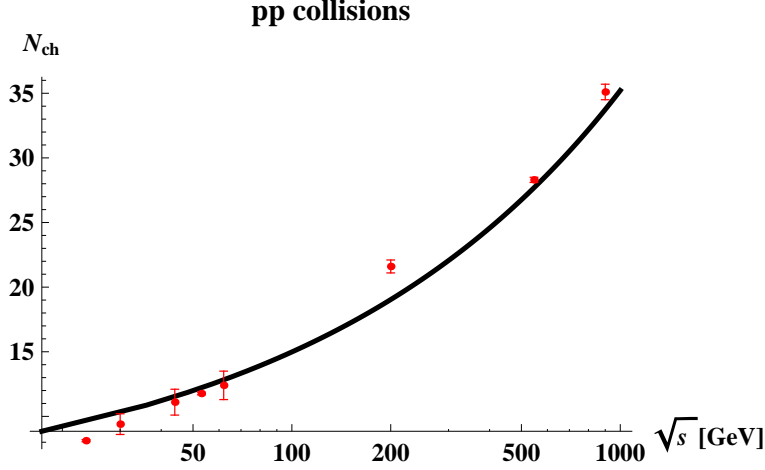


Figure 4.8: Energy dependence of the charged multiplicity for pp collisions. See text.

tum $\mathbf{Q}_s \equiv \sqrt{2}/z_s$. In holographic QCD this follows from the transcendental equation (3.77)

$$\frac{z_s}{\sqrt{2}} \mathbf{Q}_s(\chi, \mathbf{b}_\perp) = \frac{g_s^2}{2} (2\pi\alpha')^{3/2} z_a z_p \mathbf{N}(\chi, z_s, z_p, \mathbf{b}_\perp) = 1, \quad (4.16)$$

with the effective string coupling g_s and typical proton virtuality $1/z_p$. Unlike in a partonic model, the colorless wee-dipoles are the objects that saturate the transverse density.

The holographic parameters are set by the DIS data analysis, see analysis above: $\lambda = 23$, $D_\perp = 3$, $g_s = 1.5$, $z_p = 1.8 \text{ GeV}^{-1}$, $z_0 = 2 \text{ GeV}^{-1}$, $s_0 = 10^{-1} \text{ GeV}^2$.

If $A_{pp} \approx 1 \text{ fm}^2$ is the typical proton area, then $A_{pp} \mathbf{Q}_s^2 \approx 12$ is the typical number of dipoles with $\mathbf{Q}_s^2 \approx 1/2 \text{ GeV}^2$ the typical squared saturation momentum. Thus, for pp collisions the typical entropy release per unit of rapidity is

$$\mathbf{S}_{pp}/\chi \approx (A_{pp} \mathbf{Q}_s^2) \times (\mathbf{S}_1/\chi) \approx 12 \times \frac{1}{3} = 4. \quad (4.17)$$

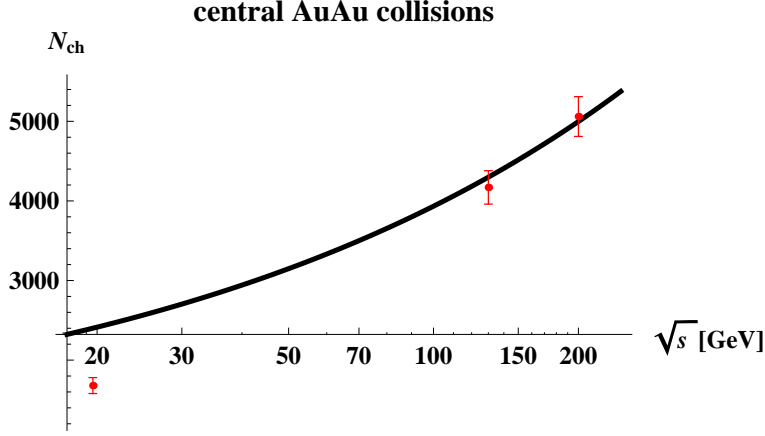


Figure 4.9: Energy dependence of the charged multiplicity for central $AuAu$ collisions. See text.

In holography, the scaling of the entropy with the energy follows from the scaling of the saturation momentum, (4.16). In the conformal limit and at large χ , the entropy asymptotes

$$\mathbf{S}_{pp} \approx \left(\frac{s}{s_0}\right)^{\left(\sqrt{1+2\sqrt{\lambda}(\alpha_P-1)}-1\right)/\sqrt{\lambda}} \ln(s/s_0), \quad (4.18)$$

which is $\mathbf{S}_{pp} \approx (s/s_0)^{0.228} \ln(s/s_0)$ using the parameters set by the DIS data. In Figure 4.8 we show the pp charged multiplicities $N_{ch,pp} = \mathbf{S}_{pp}/7.5$ [57] at collider energies [130], with $\mathbf{b}_\perp = 1/3$ fm. A recent discussion of the entropy in the context of saturation models was made in [131].

We note that for pA collisions, $A_{pA} \approx A^{1/3} A_{pp}$ so that $\mathbf{S}_{pA}/\mathbf{S}_{pp} \approx A^{1/3}$. In AA collisions, if the collision is mainly between dipoles with N-ality $k = 1$, a similar scaling with the nucleus number $A = A^{1/3} \times A^{2/3}$ is expected to take place. Here $A^{1/3}$ Lorentz contracted nucleons can be distributed in the $A^{2/3}$ transverse nucleus size. However, when the nucleons start to overlap, the $k = 2$ N-ality can be exchanged,

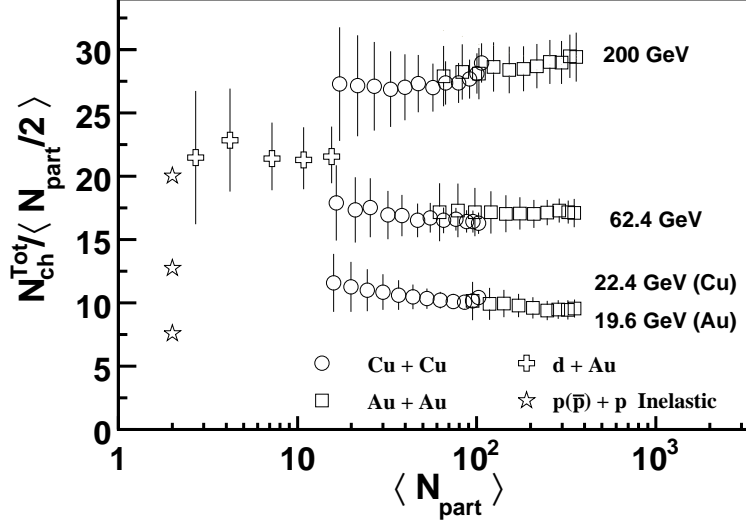


Figure 4.10: Scaling of the total charged multiplicities with the number of participants [132]. See text.

$$\frac{\mathbf{S}_{AA}}{\mathbf{S}_{pp}} \approx A \left(\sum_1^{[N_c/2]} \frac{1}{k} \right). \quad (4.19)$$

In QCD with $N_c = 3$, the sum is $3/2$. The contribution of the $k = 2$ N-ality is expected to take place when the number of participants is about 10 so that $10^{1/3} \approx 2$ corresponds to two overlapping nucleons.

In Figure 4.10 we show the total charged multiplicities normalized to the averaged number of participants as a function of the number of participants for a range of collider energies [132]. For a fixed collider energy, we note the characteristic $3/2$ jump from pp to AA collisions at a number of participants of around 10.

The charged multiplicity follows as $N_{ch,AuAu} = 3/2 \langle Au \rangle \mathbf{S}_{pp}/7.5$, with the average participating gold nucleon number $\langle Au \rangle$. Using the same numerical values as for $N_{ch,pp}$ and $\langle Au \rangle = 175$ for most central collisions [133], Figure 4.9 shows an agreement of our holographic result with the experimental data at

high energies, where the inelasticities are large. At LHC energies, we expect $N_{ch,pp} \sim 54$, $N_{ch,pPb} \sim 320$, $N_{ch,PbPb} \sim 16800$ at $\sqrt{s} = 2.76 \text{ TeV}$ and $N_{ch,pp} \sim 82$, $N_{ch,pPb} \sim 470$, $N_{ch,PbPb} \sim 23400$ at $\sqrt{s} = 7 \text{ TeV}$ using $\langle A_{PbPb} \rangle = 191$ [134].

Chapter 5

Conclusion

Dipole-dipole scattering in holographic QCD is purely imaginary at large rapidity χ which is a key feature of QCD. It follows from the t-channel exchange of closed strings induced by a prompt longitudinal “electric” field. The pomeron with N-ality 1 is a closed string exchange triggered by a stringy Schwinger mechanism. The creation process fixes the Pomeron slope and intercept in the elastic amplitude. From the open-closed string duality, Gribov’s diffusion follows from the presence of a large “electric” acceleration and the Unruh temperature causes the tachyonic mode of the dual open string to dimensionally reduce from D to D_\perp and diffuse.

In curved AdS space, the holographic direction is identified with the size (inverse virtuality) of the dipole. The idea of Gribov diffusion appears as a tachyon diffusion in both virtuality and transverse space. In the conformal limit and for $D_\perp = 3$, the dipole-dipole scattering amplitude and its related wee-dipole density are found to be identical to the QCD results for onium-onium scattering using the QCD BFKL pomeron. The results are readily extended to confining AdS with a wall and yield an explicit relation for the dipole saturation momentum as a function of rapidity χ (or equivalently $\ln(1/x)$) and impact parameter \mathbf{b}_\perp . For large impact parameter, the holographic saturation momentum is closely related to the GBW saturation momentum [41].

The dipole-dipole scattering amplitude in both conformal and confining

AdS₃ is used to analyze the F_2 structure function. A comparison with DIS data from HERA shows that the x and Q^2 dependence of our holographic result are compatible with the data in the 1-pomeron exchange approximation, with no a priori need for an eikonal multi-pomeron resummation. This conclusion is only qualitative as a more thorough study of the parameter space of the holographic model as well as the fitting accuracy are needed.

With the holographic parameters set by comparison to DIS data, we have been able to get a reasonable fit to the elastic pp scattering data and obtain a refinement of the effective dipole size z_p of the proton at large rapidities. The slope of the cross section in the region $|t| > 2 \text{ GeV}^2$ is sensitive to the IR cutoff scale, indicating the necessity of a confining background. However, the hard wall seems to be too crude an approximation for an IR cutoff. In order to fit the pp data, we need $z_p \geq z_0$ suggesting that the smooth wall background [135] is a more suitable setup. While the hard wall construct allows for explicit and analytical results, the smooth wall construct is likely numerical.

The slope parameter $B(s, |t|)$ at small momentum transfer $t \sim 1 \text{ GeV}^2$ agrees with the data and shows that our holographic model incorporates the effective proton size correctly. As is typical for diffusive processes, the mean square proton radius scales linear in rapidity. At strong coupling, the proton shrinks with increasing t'Hooft coupling.

Having fixed the parameters of the holographic model, an agreement with the DVCS data at small $|t|$ builds further confidence in the holographic approach to hadronic scattering.

We have suggested that the pomeron viewed as an exchange of an instanton on the string world-sheet carries a free energy $F_k = S_k T_U$ with S_k the instanton action of N-ality k and T_U the Unruh temperature. For large impact parameter \mathbf{b}_\perp the Unruh temperature is low and the entropy is mostly carried by the lowest string excitation, which is tachyonic. This stringy entropy is neither coherent nor thermal.

For smaller impact parameters, the Unruh temperature may reach the Hagedorn temperature, transmuting the stringy entropy to partonic entropy. The latter is likely commensurate with the Bekenstein-Hawkins entropy and

indicates the onset of a microscopic black hole. Macroscopic black holes [56–60] may be aggregates of these coalescing microscopic black holes as suggested initially in [56].

We have argued that typical pp , pA and AA collisions at current collider energies may probe this stringy entropy with low Unruh temperature. At large rapidities, the holographic entropy is in agreement with the data for the energy scaling of the charged multiplicities. The $3/2$ jump in the charged multiplicities reported by the current collider experiments with 10 participants and higher is explained by the exchange of N-ality $k = 1, 2$ strings. We expect similar jumps in the transport parameters, e.g. viscosity and flow.

Although the measured total multiplicities reflect on the final state hadronic products, entropy conservation guarantees that our prompt and initial entropy estimates are lower bounds. The general lore of energy and momentum conservation, say through viscous hydrodynamics evolution, suggests only a moderate increase of the total entropy by about 25% in going from initial to final states, making our estimates plausible.

Bibliography

- [1] I. I. Pomeranchuk *Sov. Phys. JETP* **3** (1956) 306.
- [2] I. I. Pomeranchuk and L. Okun *Sov. Phys. JETP* **3** (1956) 307.
- [3] L. L. Foldy and R. F. Peierls *Phys.Rev.* **130** (1963) 1585–1589.
- [4] F. Low *Phys.Rev.* **D12** (1975) 163–173.
- [5] S. Nussinov *Phys.Rev.Lett.* **34** (1975) 1286–1289.
- [6] L. Lipatov *Sov.J.Nucl.Phys.* **23** (1976) 338–345.
- [7] E. Kuraev, L. Lipatov, and V. S. Fadin *Sov.Phys.JETP* **45** (1977) 199–204.
- [8] I. Balitsky and L. Lipatov *Sov.J.Nucl.Phys.* **28** (1978) 822–829.
- [9] L. Gribov, E. Levin, and M. Ryskin *Phys.Rept.* **100** (1983) 1–150.
- [10] A. H. Mueller and J.-w. Qiu *Nucl.Phys.* **B268** (1986) 427.
- [11] E. Iancu and R. Venugopalan [hep-ph/0303204](#).
- [12] H. Weigert *Prog.Part.Nucl.Phys.* **55** (2005) 461–565, [hep-ph/0501087](#).
- [13] J. Jalilian-Marian and Y. V. Kovchegov *Prog.Part.Nucl.Phys.* **56** (2006) 104–231, [hep-ph/0505052](#).
- [14] F. Gelis, E. Iancu, J. Jalilian-Marian, and R. Venugopalan *Ann.Rev.Nucl.Part.Sci.* **60** (2010) 463–489, [1002.0333](#).

- [15] J. M. Maldacena *Adv.Theor.Math.Phys.* **2** (1998) 231–252,
[hep-th/9711200](#).
- [16] E. Witten *Adv.Theor.Math.Phys.* **2** (1998) 253–291, [hep-th/9802150](#).
- [17] T. Sakai and S. Sugimoto *Prog.Theor.Phys.* **113** (2005) 843–882,
[hep-th/0412141](#).
- [18] J. Erlich, E. Katz, D. T. Son, and M. A. Stephanov *Phys.Rev.Lett.* **95**
(2005) 261602, [hep-ph/0501128](#).
- [19] M. Rho, S.-J. Sin, and I. Zahed *Phys.Lett.* **B466** (1999) 199–205,
[hep-th/9907126](#).
- [20] R. Janik and R. B. Peschanski *Nucl.Phys.* **B565** (2000) 193–209,
[hep-th/9907177](#).
- [21] R. Janik and R. B. Peschanski *Nucl.Phys.* **B625** (2002) 279–294,
[hep-th/0110024](#).
- [22] R. Janik and R. B. Peschanski *Nucl.Phys.* **B586** (2000) 163–182,
[hep-th/0003059](#).
- [23] R. A. Janik *Phys.Lett.* **B500** (2001) 118–124, [hep-th/0010069](#).
- [24] G. Basar, D. E. Kharzeev, H.-U. Yee, and I. Zahed *Phys.Rev.* **D85**
(2012) 105005, [1202.0831](#).
- [25] J. Polchinski and M. J. Strassler *Phys.Rev.Lett.* **88** (2002) 031601,
[hep-th/0109174](#).
- [26] J. Polchinski and M. J. Strassler *JHEP* **0305** (2003) 012,
[hep-th/0209211](#).
- [27] R. C. Brower, J. Polchinski, M. J. Strassler, and C.-I. Tan *JHEP* **0712**
(2007) 005, [hep-th/0603115](#).
- [28] R. C. Brower, M. J. Strassler, and C.-I. Tan *JHEP* **0903** (2009) 092,
[0710.4378](#).

- [29] L. Cornalba, M. S. Costa, and J. Penedones *JHEP* **1003** (2010) 133, [0911.0043](#).
- [30] A. H. Mueller *Nucl.Phys.* **B335** (1990) 115.
- [31] A. H. Mueller *Nucl.Phys.* **B437** (1995) 107–126, [hep-ph/9408245](#).
- [32] A. H. Mueller *Nucl.Phys.* **B415** (1994) 373–385.
- [33] A. H. Mueller and B. Patel *Nucl.Phys.* **B425** (1994) 471–488, [hep-ph/9403256](#).
- [34] E. Iancu and A. Mueller *Nucl.Phys.* **A730** (2004) 460–493, [hep-ph/0308315](#).
- [35] N. N. Nikolaev and B. Zakharov *Z.Phys.* **C49** (1991) 607–618.
- [36] N. Nikolaev and B. G. Zakharov *Z.Phys.* **C53** (1992) 331–346.
- [37] G. Salam *Nucl.Phys.* **B449** (1995) 589–604, [hep-ph/9504284](#).
- [38] G. Salam *Nucl.Phys.* **B461** (1996) 512–538, [hep-ph/9509353](#).
- [39] H. Navelet, R. B. Peschanski, C. Royon, and S. Wallon *Phys.Lett.* **B385** (1996) 357–364, [hep-ph/9605389](#).
- [40] H. Navelet and S. Wallon *Nucl.Phys.* **B522** (1998) 237–281, [hep-ph/9705296](#).
- [41] K. J. Golec-Biernat and M. Wusthoff *Phys.Rev.* **D59** (1998) 014017, [hep-ph/9807513](#).
- [42] V. N. Gribov *Some Aspects of a Unified Approach to Gauge, Dual and Gribov Theories; "Gauge Theories and Quark Confinement", Moscow 2002,pp 3*.
- [43] S. J. Brodsky and G. F. de Teramond *Phys.Rev.Lett.* **96** (2006) 201601, [hep-ph/0602252](#).
- [44] S. J. Brodsky *Eur.Phys.J.* **A31** (2007) 638–644, [hep-ph/0610115](#).

- [45] M. Luscher *Nucl.Phys.* **B180** (1981) 317.
- [46] O. Aharony and M. Field *JHEP* **1101** (2011) 065, [1008.2636](#).
- [47] S. K. Domokos, J. A. Harvey, and N. Mann *Phys.Rev.* **D80** (2009) 126015, [0907.1084](#).
- [48] S. K. Domokos, J. A. Harvey, and N. Mann *Phys.Rev.* **D82** (2010) 106007, [1008.2963](#).
- [49] J.-H. Gao and B.-W. Xiao *Phys.Rev.* **D81** (2010) 035008, [0912.4333](#).
- [50] C. Marquet, C. Roiesnel, and S. Wallon *JHEP* **1004** (2010) 051, [1002.0566](#).
- [51] R. Nishio and T. Watari *Phys.Rev.* **D84** (2011) 075025, [1105.2999](#).
- [52] M. S. Costa and M. Djuric *Phys.Rev.* **D86** (2012) 016009, [1201.1307](#).
- [53] D. Kharzeev, E. Levin, and M. Nardi *Phys.Rev.* **C71** (2005) 054903, [hep-ph/0111315](#).
- [54] R. Baier, A. H. Mueller, D. Schiff, and D. Son *Phys.Lett.* **B539** (2002) 46–52, [hep-ph/0204211](#).
- [55] R. J. Fries, B. Muller, and A. Schafer *Phys.Rev.* **C79** (2009) 034904, [0807.1093](#).
- [56] E. Shuryak, S.-J. Sin, and I. Zahed *J.Korean Phys.Soc.* **50** (2007) 384–397, [hep-th/0511199](#).
- [57] S. S. Gubser, S. S. Pufu, and A. Yarom *Phys.Rev.* **D78** (2008) 066014, [0805.1551](#).
- [58] S. Lin and E. Shuryak *Phys.Rev.* **D79** (2009) 124015, [0902.1508](#).
- [59] B. Wu and P. Romatschke *Int.J.Mod.Phys.* **C22** (2011) 1317–1342, [1108.3715](#).
- [60] E. Kiritsis and A. Taliotis *JHEP* **1204** (2012) 065, [1111.1931](#).

- [61] P. L. A. Donnachie, G. Dosch and O. Nachtmann *Cambridge University Press, Cambridge* (2002).
- [62] E. Shuryak and I. Zahed [1301.4470](#).
- [63] V. N. Gribov *Proceedings 8th LNPI Winter School on Nuclear and Elementary Particle Physics, pp 5 (1973)*.
- [64] O. Andreev and W. Siegel *Phys.Rev.* **D71** (2005) 086001, [hep-th/0410131](#).
- [65] O. Andreev *Phys.Rev.* **D71** (2005) 066006, [hep-th/0408158](#).
- [66] Y. Hatta, E. Iancu, and A. Mueller *JHEP* **0801** (2008) 063, [0710.5297](#).
- [67] Y. Hatta, E. Iancu, and A. Mueller *JHEP* **0801** (2008) 026, [0710.2148](#).
- [68] J. L. Albacete, Y. V. Kovchegov, and A. Taliotis *JHEP* **0807** (2008) 074, [0806.1484](#).
- [69] J. L. Albacete, Y. V. Kovchegov, and A. Taliotis *AIP Conf.Proc.* **1105** (2009) 356–360, [0811.0818](#).
- [70] L. Cornalba and M. S. Costa *Phys.Rev.* **D78** (2008) 096010, [0804.1562](#).
- [71] L. Cornalba, M. S. Costa, and J. Penedones *Phys.Rev.Lett.* **105** (2010) 072003, [1001.1157](#).
- [72] O. Nachtmann *Annals Phys.* **209** (1991) 436–478.
- [73] O. Nachtmann [hep-ph/9609365](#).
- [74] G. P. Korchemsky *Phys.Lett.* **B325** (1994) 459–466, [hep-ph/9311294](#).
- [75] A. Shoshi, F. Steffen, and H. Pirner *Nucl.Phys.* **A709** (2002) 131–183, [hep-ph/0202012](#).
- [76] A. Kramer and H. G. Dosch *Phys.Lett.* **B252** (1990) 669–675.

- [77] H. G. Dosch, E. Ferreira, and A. Kramer *Phys.Rev.* **D50** (1994) 1992–2015, [hep-ph/9405237](#).
- [78] V. Barone and E. Predazzi *High-Energy Particle Diffraction*, Springer, Berlin (2002).
- [79] F. Wegner *J.Math.Phys.* **12** (1971) 2259–2272.
- [80] K. G. Wilson *Phys.Rev.* **D10** (1974) 2445–2459.
- [81] J. M. Maldacena *Phys.Rev.Lett.* **80** (1998) 4859–4862, [hep-th/9803002](#).
- [82] S.-J. Rey and J.-T. Yee *Eur.Phys.J.* **C22** (2001) 379–394, [hep-th/9803001](#).
- [83] J. Greensite and P. Olesen *JHEP* **9808** (1998) 009, [hep-th/9806235](#).
- [84] J. Greensite and P. Olesen *JHEP* **9904** (1999) 001, [hep-th/9901057](#).
- [85] D. E. Berenstein, R. Corrado, W. Fischler, and J. M. Maldacena *Phys.Rev.* **D59** (1999) 105023, [hep-th/9809188](#).
- [86] D. J. Gross and H. Ooguri *Phys.Rev.* **D58** (1998) 106002, [hep-th/9805129](#).
- [87] K. Zarembo *Phys.Lett.* **B459** (1999) 527–534, [hep-th/9904149](#).
- [88] J. Sonnenschein and A. Loewy *JHEP* **0001** (2000) 042, [hep-th/9911172](#).
- [89] G. Veneziano *Nucl.Phys.* **B117** (1976) 519–545.
- [90] E. Meggiolaro *Z.Phys.* **C76** (1997) 523–535, [hep-th/9602104](#).
- [91] E. Meggiolaro *Eur.Phys.J.* **C4** (1998) 101–106, [hep-th/9702186](#).
- [92] S. Fubini, D. Gordon, and G. Veneziano *Phys.Lett.* **B29** (1969) 679–682.

- [93] J. Greensite *Prog.Part.Nucl.Phys.* **51** (2003) 1, [hep-lat/0301023](#).
- [94] M. Froissart *Phys.Rev.* **123** (1961) 1053–1057.
- [95] V. Gribov and L. Lipatov *Sov.J.Nucl.Phys.* **15** (1972) 438–450.
- [96] A. M. Polyakov *Phys.Lett.* **B103** (1981) 207–210.
- [97] U. H. Danielsson, E. Keski-Vakkuri, and M. Kruczenski *JHEP* **9901** (1999) 002, [hep-th/9812007](#).
- [98] J. R. David, M. R. Gaberdiel, and R. Gopakumar *JHEP* **1004** (2010) 125, [0911.5085](#).
- [99] G. Altarelli and G. Parisi *Nucl.Phys.* **B126** (1977) 298.
- [100] Y. L. Dokshitzer *Sov.Phys.JETP* **46** (1977) 641–653.
- [101] I. Balitsky *Nucl.Phys.* **B463** (1996) 99–160, [hep-ph/9509348](#).
- [102] Y. V. Kovchegov *Phys.Rev.* **D61** (2000) 074018, [hep-ph/9905214](#).
- [103] Y. V. Kovchegov *Phys.Rev.* **D60** (1999) 034008, [hep-ph/9901281](#).
- [104] G. Soyez *Braz.J.Phys.* **36** (2006) 1194–1203, [hep-ph/0605192](#).
- [105] R. C. Brower, M. Djuric, I. Sarcevic, and C.-I. Tan *JHEP* **1011** (2010) 051, [1007.2259](#).
- [106] R. C. Brower, M. Djuric, I. Sarcevic, and C.-I. Tan [1106.5681](#).
- [107] P. Tribedy and R. Venugopalan *Nucl.Phys.* **A850** (2011) 136–156, [1011.1895](#).
- [108] C. Schubert *J.Phys.Conf.Ser.* **287** (2011) 012031, [1103.0243](#).
- [109] J. S. Schwinger *Phys.Rev.* **82** (1951) 664–679.
- [110] W. Unruh *Phys.Rev.* **D14** (1976) 870.

- [111] D. Kharzeev and K. Tuchin *Nucl.Phys.* **A753** (2005) 316–334, [hep-ph/0501234](#).
- [112] A. Strominger and C. Vafa *Phys.Lett.* **B379** (1996) 99–104, [hep-th/9601029](#).
- [113] L. Susskind [hep-th/9309145](#).
- [114] G. T. Horowitz and J. Polchinski *Phys.Rev.* **D55** (1997) 6189–6197, [hep-th/9612146](#).
- [115] R. R. Khuri *Nucl.Phys.* **B588** (2000) 253–262, [hep-th/0006063](#).
- [116] L. Susskind *Phys.Rev.* **D49** (1994) 6606–6611, [hep-th/9308139](#).
- [117] Y. V. Kovchegov, Z. Lu, and A. H. Rezaeian *Phys.Rev.* **D80** (2009) 074023, [0906.4197](#).
- [118] **H1 and ZEUS Collaboration** Collaboration, F. Aaron *et al.* *JHEP* **1001** (2010) 109, [0911.0884](#).
- [119] M. Good and W. Walker *Phys.Rev.* **120** (1960) 1857–1860.
- [120] M. Ryskin, A. Martin, and V. Khoze *Eur.Phys.J.* **C72** (2012) 1937, [1201.6298](#).
- [121] M. Wirbel, B. Stech, and M. Bauer *Z.Phys.* **C29** (1985) 637.
- [122] U. Amaldi and K. R. Schubert *Nucl.Phys.* **B166** (1980) 301.
- [123] A. Donnachie and P. Landshoff [1112.2485](#).
- [124] I. Dremin [1206.5474](#).
- [125] N. A. Amos, M. Block, G. Bobbink, M. Botje, D. Favart, *et al.* *Nucl.Phys.* **B262** (1985) 689.
- [126] **UA4 Collaboration** Collaboration, . Bernard, Denis *et al.* *Phys.Lett.* **B198** (1987) 583.

- [127] **H1 Collaboration** Collaboration, F. Aaron *et al.* *Phys.Lett.* **B659** (2008) 796–806, [0709.4114](#).
- [128] **ZEUS Collaboration** Collaboration, S. Chekanov *et al.* *JHEP* **0905** (2009) 108, [0812.2517](#).
- [129] **H1 Collaboration** Collaboration, F. Aaron *et al.* *Phys.Lett.* **B681** (2009) 391–399, [0907.5289](#).
- [130] M. Basile, G. Cara Romeo, L. Cifarelli, A. Contin, G. D’Ali, *et al.* *Nuovo Cim.* **A65** (1981) 400.
- [131] K. Kutak *Phys.Lett.* **B705** (2011) 217–221, [1103.3654](#).
- [132] B. Alver, B. Back, M. Baker, M. Ballintijn, D. Barton, *et al.* *Phys.Rev.Lett.* **102** (2009) 142301, [0709.4008](#).
- [133] B. Back, M. Baker, D. Barton, R. Betts, M. Ballintijn, *et al.* *Phys.Rev.Lett.* **91** (2003) 052303, [nucl-ex/0210015](#).
- [134] **ALICE Collaboration** Collaboration, K. Aamodt *et al.* *Phys.Rev.Lett.* **106** (2011) 032301, [1012.1657](#).
- [135] A. Karch, E. Katz, D. T. Son, and M. A. Stephanov *Phys.Rev.* **D74** (2006) 015005, [hep-ph/0602229](#).